

Journal of Medical Imaging

MedicalImaging.SPIEDigitalLibrary.org

Numerical observer for atherosclerotic plaque classification in spectral computed tomography

Auranuch Lorsakul
Georges El Fakhri
William Worstell
Jinsong Ouyang
Yothin Rakvongthai
Andrew F. Laine
Quanzheng Li

SPIE.

Auranuch Lorsakul, Georges El Fakhri, William Worstell, Jinsong Ouyang, Yothin Rakvongthai, Andrew F. Laine, Quanzheng Li, "Numerical observer for atherosclerotic plaque classification in spectral computed tomography," *J. Med. Imag.* 3(3), 035501 (2016), doi: 10.1117/1.JMI.3.3.035501.

Numerical observer for atherosclerotic plaque classification in spectral computed tomography

Auranuch Lorsakul,^{a,b} Georges El Fakhri,^{a,c} William Worstell,^d Jinsong Ouyang,^{a,c} Yothin Rakvongthai,^{a,e} Andrew F. Laine,^b and Quanzheng Li^{a,c,*}

^aMassachusetts General Hospital, Division of Nuclear Medicine and Molecular Imaging, Gordon Center for Medical Imaging, 55 Fruit Street, White 427, Boston, Massachusetts 02114, United States

^bColumbia University, Department of Biomedical Engineering, 1210 Amsterdam Avenue, New York, New York 10027, United States

^cHarvard Medical School, Department of Radiology, 25 Shattuck Street, Boston, Massachusetts 02115, United States

^dPhotoDiagnostic System Inc., 85 Swanson Road, Boxborough, Massachusetts 01719, United States

^eChulalongkorn University, Department of Radiology, Faculty of Medicine, 1873 Rama 4 Road, Pathumwan, Bangkok 10330, Thailand

Abstract. Spectral computed tomography (SCT) generates better image quality than conventional computed tomography (CT). It has overcome several limitations for imaging atherosclerotic plaque. However, the literature evaluating the performance of SCT based on objective image assessment is very limited for the task of discriminating plaques. We developed a numerical-observer method and used it to assess performance on discrimination vulnerable-plaque features and compared the performance among multienergy CT (MECT), dual-energy CT (DECT), and conventional CT methods. Our numerical observer was designed to incorporate all spectral information and comprised two-processing stages. First, each energy-window domain was preprocessed by a set of localized channelized Hotelling observers (CHO). In this step, the spectral image in each energy bin was decorrelated using localized prewhitening and matched filtering with a set of Laguerre–Gaussian channel functions. Second, the series of the intermediate scores computed from all the CHOs were integrated by a Hotelling observer with an additional prewhitening and matched filter. The overall signal-to-noise ratio (SNR) and the area under the receiver operating characteristic curve (AUC) were obtained, yielding an overall discrimination performance metric. The performance of our new observer was evaluated for the particular binary classification task of differentiating between alternative plaque characterizations in carotid arteries. A clinically realistic model of signal variability was also included in our simulation of the discrimination tasks. The inclusion of signal variation is a key to applying the proposed observer method to spectral CT data. Hence, the task-based approaches based on the signal-known-exactly/background-known-exactly (SKE/BKE) framework and the clinical-relevant signal-known-statistically/background-known-exactly (SKS/BKE) framework were applied for analytical computation of figures of merit (FOM). Simulated data of a carotid-atherosclerosis patient were used to validate our methods. We used an extended cardiac-torso anthropomorphic digital phantom and three simulated plaque types (i.e., calcified plaque, fatty-mixed plaque, and iodine-mixed blood). The images were reconstructed using a standard filtered backprojection (FBP) algorithm for all the acquisition methods and were applied to perform two different discrimination tasks of: (1) calcified plaque versus fatty-mixed plaque and (2) calcified plaque versus iodine-mixed blood. MECT outperformed DECT and conventional CT systems for all cases of the SKE/BKE and SKS/BKE tasks (all $p < 0.01$). On average of signal variability, MECT yielded the SNR improvements over other acquisition methods in the range of 46.8% to 65.3% (all $p < 0.01$) for FBP-Ramp images and 53.2% to 67.7% (all $p < 0.01$) for FBP-Hanning images for both identification tasks. This proposed numerical observer combined with our signal variability framework is promising for assessing material characterization obtained through the additional energy-dependent attenuation information of SCT. These methods can be further extended to other clinical tasks such as kidney or urinary stone identification applications. © 2016 Society of Photo-Optical Instrumentation Engineers (SPIE) [DOI: 10.1117/1.JMI.3.3.035501]

Keywords: numerical observer; channelized Hotelling observer; spectral computed tomography; classification task; plaque imaging; image quality assessment.

Paper 15252R received Feb. 23, 2016; accepted for publication Jun. 20, 2016; published online Jul. 12, 2016.

1 Introduction

Atherosclerosis-related cerebrovascular (CV) and cardiovascular events, such as ischemic stroke and myocardial infarction, are the major leading causes of morbidity and mortality worldwide.^{1,2} The presence of atherosclerotic plaque is an independent predictor of risk for these events. For example, plaques with certain morphologies have a prognostic value independent

of and incremental to the presence or absence of luminal obstruction (stenosis) associated with the plaque.³ It is also known that the prevalence of severe carotid artery stenosis is a predictor of poorer CV outcome and that it increases progressively concurrent with coronary artery stenosis.¹ Therefore, the detection of plaque and assessment of its vulnerability are crucial for calculating the risk for stroke and sudden cardiac death. In particular, plaque vulnerability can be assessed by resolving

*Address all correspondence to: Quanzheng Li, E-mail: li.quanzheng@mgh.harvard.edu

several features, including thin cap fibroatheroma, large lipid core, intimal spotty calcification, positive remodeling, and intra-plaque neovascularization.⁴ Low-grade stenosis may also be associated with increased risk of the future acute events involving carotid and coronary arteries, so determination of plaque features beyond the degree of stenosis is important.⁵ Thus, for each imaging examination, it is not only necessary to identify plaques that create luminal obstructions but also necessary to interpret and characterize plaques that typically form within the arterial vascular system.

Conventional computed tomography (CT) and CT angiography (CTA) are well-established techniques that are frequently used for the detection and characterization of calcifications within vessel walls.⁶ CTA provides an absolute (average) quantitative measure of tissue composition and enables grading of the severity of stenosis when evaluating stroke patients.⁷ Although the detection and quantification of calcium can be performed with high accuracy using CT, this method is still deficient in its ability to characterize different constituents of mixed or purely noncalcified plaques, particularly in smaller plaques and vessels.⁸ Typically, CT may be limited in its ability to clearly distinguish plaques from surrounding soft tissues or from contrast agents, since each may yield the same x-ray attenuation coefficient and thus the same grayscale value of CT number or Hounsfield unit (HU). For example, calcified plaques and iodine in a contrast-filled vessel are chemically distinct, but they can have similar x-ray attenuation integrals, which can render them difficult to distinguish in a CT image. Consequently, the major limitations of CT are: (1) an insufficient contrast between different soft tissues for some clinical tasks, in particular relative to MRI; (2) a lack of specificity when distinguishing different tissues, which may present with similar pixel intensities; (3) the relatively high-dose nature of CT scanning as compared to other image modalities (e.g., MRI); and (4) frequently provided qualitative grayscale pixel values of CT images, rather than quantitative linear attenuation coefficients.⁹ These shortcomings of CT may consequently hinder the proper assessment, differentiation, and characterization of the various structures and features important to plaque imaging.

Spectral CT, which generates additional material-different information by collecting data using more than one single-source energy spectrum, shows promise for mitigating several limitations of conventional CT. Spectral CT improves material differentiation by combining CT techniques with measurement of the energy-dependent (i.e., spectral) attenuation properties of the examined tissues.¹⁰ Dual-energy CT (DECT) is the simplest and currently most broadly used implementation of spectral CT. Several types of DECT systems have been designed that make use of different technical approaches, including dual-source CT, e.g., Somatom Definition and Somatom Definition Flash (both by Siemens Healthcare; Forchheim, Germany), fast kVp-switching CT, e.g., GE Discovery CT750HD (GE Healthcare; Milwaukee, Wisconsin) or dual-layer CT, e.g., Brilliance 64-channel CT (Philips Research; Hamburg, Germany).

Although it makes use of the additional spectral information obtained through use of these several designs, current DECT technology still achieves only limited performance in plaque imaging. Specifically, DECT can offer high spatial resolution for plaque morphology measurement, but current limitations arise in the differentiation of materials with DECT when the two energy spectra used have a significant overlap.⁹ In addition, DECT, such as dual-source CT, sometimes requires relatively

high dose levels as compared to conventional CT,¹¹ and it is not safe for sequential studies.¹² As a result, these limitations currently exclude DECT from widespread use in several clinical applications and from serial studies in plaque imaging.

In contrast to DECT, multienergy CT (MECT) with well-defined multiple spectral windows potentially offers a higher degree of material specificity when distinguishing components of vulnerable atherosclerotic plaque through their energy responses. MECT has potential to better characterize and quantify the concentration of the plaque components (e.g., water, lipid, and calcium) as well as various contrast agents (e.g., iodine, gadolinium, and gold) relative to DECT.^{4,12} The photon-counting detector approach is one technical strategy to implementing MECT, since it can allow more than the two-energy windows available in DECT. CT based on photon-counting detectors measures each incident x-ray photon as it interacts with the detector and generates an electronic signal, with the measured event then accumulated into different bins based on the measured photon energy. Through the rapid progress of detector technologies in the last decade, several vendors have offered CT systems with both clinical and preclinical geometries, e.g., LightSpeed VCT (GE Healthcare; Waukesha, Wisconsin), Somatom Definition AS (Siemens Healthcare; Forchheim, Germany), and the preclinical PCD-CT (Philips Research; Hamburg, Germany). Alternative designs for MECT systems may employ *K*-edge filters, and, in one instance, used multiple balanced *K*-edge filters.¹³

By means of energy-resolved devices, which can provide more accurate tissue characterization and quantification, MECT holds the promise to several clinical demands in atherosclerotic plaque characterization including: (1) improving the contrast-to-noise ratio and contrast of CT images; (2) reducing the dose of x-ray radiation and contrast agents due to the ability to achieve a comparable contrast-to-noise ratio at lower dose efficiency when compared to DECT and conventional CT;^{14,15} (3) providing better quantitative using well-defined energies; (4) allowing accurate *K*-edge imaging; (5) allowing simultaneous multiagent imaging; (6) enabling molecular CT with nanoparticle contrast agents and personalized medicine.⁹ With these capabilities, MECT images are being investigated and evaluated to be ready for clinical use.

To evaluate the performance of imaging systems, it is important that image quality be assessed in the framework of average performance of inference tasks by observers or decision-makers.¹⁶ Such an approach has become known as objective image assessment. Objective assessment consists of: (1) specification of a task; (2) description of the data (e.g., object classes and imaging process); (3) depiction of the observer; and (4) assessment of a figure of merit.¹⁶ Fundamentally, modeling the performance of a human observer, e.g., a radiologist or a nuclear medicine physician, is the standard goal for objective image assessment. However, having a human observer performed the tasks for imaging system evaluation is costly and time-consuming, because the human-performance task assessment of a particular scanner or scanning protocol requires tremendous amount of data and the assistance of several radiologists. Alternatively, models of human observers using a computer (numerical) observer, i.e., Hotelling observers (HOs), can be used to reduce time and cost of human-observer studies. The HO is a well-known numerical observer that uses estimation of image statistics to quantify the observer performance, thereby predicting human performance.^{17–20} It requires only the first- and second-order statistics of the data to maximize the

signal-to-noise ratio (SNR), which is a common figure-of-merit (FOM) measure of observer performance. The HO constrained to a number of channels (linear filters) is called the channelized-Hotelling observer (CHO).²¹ The channels can properly extract the efficient features that preserve maximal information in the data using spatial-frequency-selective and orientation-selective mechanisms. There is a substantial body of work demonstrating that HO and CHO correlates well with human performance. As a result, they are usually selected as a common metric for objective evaluation and comparison of medical imaging systems.^{17,20,22–27}

Objective image assessment of the performance improvement obtained using spectral CT is mainly limited to investigation of particular clinical tasks. Several studies have shown that material decomposition with spectral CT imaging provides better differentiation of materials for atherosclerotic plaque features.^{4,12,28–31} Nonetheless, there are limited studies of quantitative metrics for evaluating performance in terms of objective image assessment exploiting a numerical observer in spectral CT imaging.³² The major problems may be because it is difficult to correlate the data from different energy bins, especially given the complexity of the spectral CT data, since spectral CT imaging can be considered a four-dimensional (4-D) technique to form measurements in three spatial dimensions and a unique energy dimension.³³ Occasionally, a current evaluation of DECT is performed on energy-subtracted images (i.e., the subtraction between low- and high-energy images). In the available scientific literature, the subtracted images, however, resulted in inferior image quality owing to signal lost (reduced photon counts) and increased image noise (variance).^{34–36} In diagnostic evaluation, subtraction causes difficulty in the quantitative and qualitative analyses of plaque images. This is because the possible erroneous subtraction of small, focal calcifications may partly affect diagnostic accuracy. For these reasons, it is suboptimal to evaluate the observer performance on subtracted images of DECT. Since the inclusion of useful information from all energy bins of spectral CT is crucial in characterizing the plaque components, a numerical observer that incorporates contributions from all this information is essential for fully objective assessment of spectral CT images.

In this study, we developed a numerical observer that incorporated multiple spectral information and a quantitative FOM, which could be used in the material discrimination for evaluating spectral CT imaging systems, including DECT and MECT. Then, we compared the classification performance among spectral CT (i.e., DECT and MECT) and conventional CT. Specifically, the proposed numerical observer accounted for all spectral information, not limited only to two energy spectra but rather incorporating several multiple energy spectra. For spectral CT, we mimicked the detection performance of a radiologist browsing through the individual bin images. Specifically, this observer design was similar to the way that a radiologist views multiple energy windows of spectral CT images to investigate attenuation values of a tissue at multiple energy levels. In the study reported by Saba et al.,²⁸ they showed that the HU values of each plaque type (e.g., fatty, mixed, and calcified) should be classified according to the energy level because the HU values of plaque significantly change with the selected kiloelectron volt. Our observer design was motivated by Platasa et al. and Chen et al., who built and validated a sophisticated two-layered numerical observer.^{37,38} In addition, our recent studies demonstrated that the use of additional signal

information in numerical observers could lead to more accurate image assessment.^{39–42} These studies encouraged us to apply the proposed numerical observer to evaluate the discrimination performance using spectral CT images incorporating the extra spectral information. Our method can be used to evaluate the maximal performance that may be obtained using the spectral CT technology, whose additional spectral information enhances the material characterization. In this work, we performed the carotid-plaque discrimination task of deciding which of the two plaque features (e.g., calcified plaque and fatty-mixed plaque) was present in a known background. Similar to the signal-detection approach, the material classification (or discrimination) task falls within the same category of a “decision task” in imaging literature, as the observer decides based on the given signal contrast which of the two materials was present.¹⁶ In this study, we performed the plaque discrimination task based on: (1) the signal-known-exactly/background-known-exactly (SKE/BKE) framework and (2) the signal-known-statistically/background-known-exactly (SKS/BKE) framework. Basically, the SKE/BKE task is widely used due to its convenience and simplicity as the signal is assumed to be a known deterministic entity to the observer, i.e., all parameters characterizing the signal location, size, shape, and known properties of the background noise. Unlike the SKE/BKE paradigm, the SKS/BKE paradigm is able to mimic clinical-oriented scenarios as the signal incorporates randomness through a statistically defined distribution and associating parameters not known to the observer (e.g., with signal variability in plaque diameters or concentrations).⁴³ This approach corresponded to the clinical practice of plaque imaging, as with the degree of stenosis or variation in intraluminal diameters of the plaque possibly altered and task performance assessed as a function of changes of tube voltage levels in CT imaging.³⁰

The validation of our approach was performed using simulated data. A digital anthropomorphic phantom (i.e., extended cardiac-torso, XCAT) was used to generate attenuation coefficient maps together with vulnerable carotid plaques. The plaque features with known compositions, including calcification, fat mixed (noncalcification), and iodine mixed, were separately generated and inserted into the vulnerable carotid plaques of the phantom background. Poisson-distributed noise was added to the projected sinograms, which were reconstructed to be investigated images using the filtered backprojection (FBP) algorithm. The classification performance was compared among the MECT (photon counting), DECT (dual-source, kVp-switching), and conventional (80, 120, and 140 kVp) CT systems at equivalent dose.

2 Materials and Methods

2.1 Assessment of Binary Material Classification

We studied a binary discrimination task, which was determined by two material hypotheses composed in the signal contrasts (i.e., H_1 and H_2). An observer decided which of the two hypotheses was true from a spectral CT image. Let us denote \mathbf{s}_i as the material $i = \{1, 2\}$ to be detected, \mathbf{b} as the noiseless image background, and \mathbf{n} as the measured noise in the image. Then the image, \mathbf{g} , under the two hypotheses can be expressed as

$$H_1 : \mathbf{g} = \mathbf{b} + \mathbf{n} + \mathbf{s}_1, \quad (1)$$

$$H_2 : \mathbf{g} = \mathbf{b} + \mathbf{n} + \mathbf{s}_2. \quad (2)$$

The performance of separating the two materials could be expressed in terms of the observer's SNR and area under the receiver operating characteristic curve (AUC).

2.1.1 Signal-known-exactly and background-known-exactly (SKE/BKE) discrimination task

The material classification task was performed to discriminate between two composite materials in carotid plaques (e.g., calcium and mixed fat) based on the standard detection of SKE/BKE. For a quantitative system evaluation, SKE/BKE provides a useful model of an interesting object as a known deterministic contribution of signal (i.e., based on size, shape, contrast, and location) together with statistically known background given to the observer.⁴³ The determination task was to classify which of the two materials in the image was comprised based on the observed signal contrast, and this resulted in the FOM of the discrimination performance. The SKE detection tasks served as a good starting point for investigating the signal discrimination task; however, this simplified task was not clinically realistic, since the observed material density or concentration might not be constant in the human body.

2.1.2 Signal-known-statistically and background-known-exactly (SKS/BKE) discrimination task

To mimic a scenario in clinical practice, a more clinically relevant framework of task-based assessment to compare the performance on spectral CT imaging was proposed. In the straightforward SKE/BKE paradigm, the FOM is higher if higher signal-to-noise is simply satisfied. In addition to SKE/BKE, we explored the SKS/BKE task that allowed variability in the signal.^{32,43} In contrast to SKE/BKE, the additional signal uncertainty specified by a statistically defined distribution was incorporated to investigate a more complex plaque-feature discrimination task. The density of the carotid plaque features to be investigated was varied according to specified statistical distribution. The shape of the plaque was known but its density or concentration was not precisely known. In this study, the plaque feature present in the carotid vulnerable region was defined as a circular shape and its diameter was varied as a Gaussian-distributed function. The observer decided which of the two material hypotheses was true at a known location in each signal uncertainty. This SKS/BKE model incorporated the signal uncertainty yielded a more clinically relevant task for quantitative assessment of the spectral CT systems.

2.2 Numerical Observer

We proposed to develop a numerical observer that accommodated multiple energy bins of spectral CT images. The proposed numerical observer included two processing stages as shown in Fig. 1. First, the preprocessing stage accounted for the spectral information in each energy bin using a CHO model. Each spectral CT image of each energy bin was channelized and then the two-dimensional (2-D) CHO was computed for all spectral CT bins to yield arrays of the intermediate scores of the decision variables. The second stage was the integration phase that combined the information of the decision variables, extracted from all energy bins, by using an additional one-dimensional (1-D) HO model. The decision variable arrays were applied to the HO and, then, FOMs of discrimination SNR and AUC were

determined, which could be used to measure the observer performance based on the totality of spectral CT images.

2.2.1 Preprocessing stage

A CHO model accommodated each spectral CT image of all energy bins in the preprocessing stage. Let an image, \mathbf{g} , under consideration be denoted by a 2-D vector, $\mathbf{f}_{(n,j)}$, $n = \{1, \dots, N\}$, of the intensity of image N pixels in 2-D data. Then, denote $j = \{1, \dots, J\}$ as the energy bin of a spectral CT image for the total J energy bins. The spectral CT image was first processed with a set of 2-D channels to extract the main features and yielded a channel output. A channel matrix, $\mathbf{U} = [\mathbf{u}_1, \mathbf{u}_2, \dots, \mathbf{u}_p]$, was formed by a channel \mathbf{u}_p , $p = \{1, \dots, P\}$, where P is the number of channels. In energy bin j , each image, \mathbf{f} , was channelized by the set of P channels to result a channel output, \mathbf{v} , as

$$\mathbf{v}_{(i,j)} = \mathbf{U}^T \mathbf{f}_{(n,j)}^i, \quad (3)$$

where the operator T is the matrix transpose and i is the investigated material.

In selecting the channels for the present study, we referred to the primary objective of validation of the observer framework rather than their ability to mimic humans. Accordingly, we chose 2-D Laguerre–Gauss channels (LG) that yielded rotationally symmetric square-integrable functions with no preferred orientation in the correlation structure of the signal. These channels operated the image for the feature extraction to reduce the dimensionality problem, thereby increasing computation feasibility. The LG channels had comparable performance to difference-of-Gaussian channels, which had ability to mimic human visual systems, for investigating spherical targets.⁴⁰ The LG functions are the product of Laguerre polynomials and Gaussian function defined as

$$u_p(r|d_u) = \frac{\sqrt{2}}{d_u} \exp\left(\frac{-\pi r^2}{d_u^2}\right) \mathfrak{L}_p\left(\frac{2\pi r^2}{d_u^2}\right), \quad (4)$$

where $r \in \mathfrak{R}^2$, d_u is the spread parameter, and \mathfrak{L}_p denotes Laguerre polynomials defined as $\mathfrak{L}_p(q) = \sum_{k=0}^p (-1)^k \binom{p}{k} \frac{q^k}{k!}$.

The channelized data were employed to estimate 2-D CHO template of each energy bin. Within an individual spectral image, the CHO template, $\mathbf{W}_{\text{CHO}(j)}$, was then constructed using a localized prewhitening process to decorrelate signals; and a localized matched filter to detect the presence of signals embedded in noise, defined as

$$\mathbf{W}_{\text{CHO}(j)} = \mathbf{K}_{\mathbf{v}_{(i,j)}}^{-1} \Delta \bar{\mathbf{v}}_{(i,j)}, \quad (5)$$

where $\mathbf{K}_{\mathbf{v}_{(i,j)}} = \mathbf{U}^T \mathbf{K}_{\mathbf{f}_{(n,j)}} \mathbf{U}$ is the channelized covariance matrix of $\mathbf{K}_{\mathbf{f}_{(n,j)}} = (1/2)(\mathbf{K}_{\mathbf{f}_{(n,j)}^1} + \mathbf{K}_{\mathbf{f}_{(n,j)}^2})$, denoted as the average covariance matrix of the two material hypotheses composed in the signal contrasts; $\Delta \bar{\mathbf{v}}_{(i,j)} = \mathbf{U}^T \Delta \bar{\mathbf{f}}_{(n,j)}$ is the matched filter computed from the mean difference of the image vectors, $\Delta \bar{\mathbf{f}}_{(n,j)} = \langle \mathbf{f}_{(n,j)}^i | H_2 \rangle - \langle \mathbf{f}_{(n,j)}^1 | H_1 \rangle$, for the two material hypotheses composed in the signal contrasts. The operator $\langle \cdot \rangle$ denotes the ensemble average. Note that the covariance matrix of each hypothesis is the ensemble average over all noise realizations, which describes the randomness of background variability and

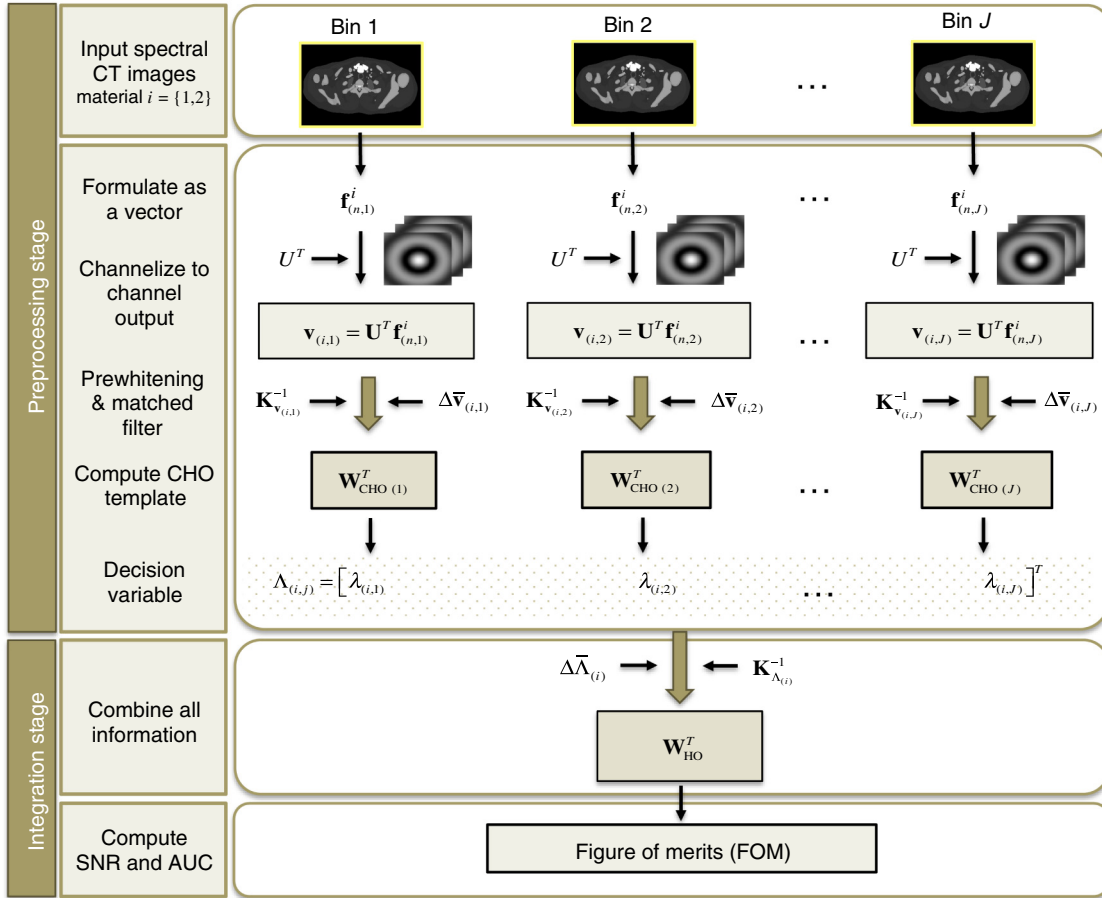


Fig. 1 The design of the proposed numerical observer for spectral CT images. In the figure, $\mathbf{f}_{(n,j)}$ is the vector representing the image within the region of interest (ROI), n is the number of voxels in the ROI, i is the material index. Top row, two material images for each energy bin are input and \mathbf{U}^T is the channel matrix, where the operator T is the matrix transpose.

measurement noise, denoted as $\mathbf{K}_{\mathbf{f}_{(n,j)}} = \langle [\mathbf{f}_{(n,j)}^i - \bar{\mathbf{f}}_{(n,j)}^i][\mathbf{f}_{(n,j)}^i - \bar{\mathbf{f}}_{(n,j)}^i]^T | H_i \rangle$, $i = \{1,2\}$.

Next, the 2-D CHO templates were then applied to calculate the intermediate decision variable, λ , for each energy bin j . The output decision variables of all energy bins were stored as a vector of decision variables, $\Lambda_{(i,j)} = [\lambda_{(i,1)}, \lambda_{(i,2)}, \dots, \lambda_{(i,J)}]^T$. The intermediate decision variable was defined as

$$\lambda_{(i,j)} = \mathbf{W}_{\text{CHO}(j)}^T \mathbf{v}_{(i,j)}. \quad (6)$$

2.2.2 Integration stage

This step integrated the decision variable arrays of all energy bins. Both material hypotheses were computed to form the intermediate score arrays $\Lambda_{(i,j)} = [\lambda_{(i,1)}, \lambda_{(i,2)}, \dots, \lambda_{(i,J)}]^T | H_i$, $i = \{1,2\}$. These score arrays were input to a 1-D HO model, which was used to construct the observer template. The integrated HO template was computed as

$$\mathbf{W}_{\text{HO}} = \mathbf{K}_{\Lambda}^{-1} \Delta \bar{\Lambda}, \quad (7)$$

where $\mathbf{K}_{\Lambda} = (1/2)[\mathbf{K}_{\Lambda(1,j)} + \mathbf{K}_{\Lambda(2,j)}]$ is the average covariance matrix of the decision variable arrays for the two material hypotheses composed in the signal contrasts; $\Delta \bar{\Lambda} = \langle \Lambda_{(i,j)} | H_2 \rangle - \langle \Lambda_{(i,j)} | H_1 \rangle$ is a matched filter computed from

mean difference of the decision variable arrays over all noise realizations. Note that the covariance matrix of each hypothesis is the ensemble average over all noise realizations, denoted as $\mathbf{K}_{\Lambda_{(i,j)}} = \langle [\Lambda_{(i,j)} - \bar{\Lambda}_{(i,j)}][\Lambda_{(i,j)} - \bar{\Lambda}_{(i,j)}]^T | H_i \rangle$, $i = \{1,2\}$.

Finally, the FOMs of the discrimination SNR that completely integrated the information of the entire energy bins was computed as

$$\text{SNR} = (\Delta \bar{\Lambda}^T \mathbf{K}_{\Lambda}^{-1} \Delta \bar{\Lambda}), \quad (8)$$

and the corresponding AUC was calculated as

$$\text{AUC} = \frac{1}{2} + \frac{1}{2} \text{erf} \left(\frac{\text{SNR}}{2} \right), \quad (9)$$

where $\text{erf}(x)$ is the Gauss error function.

Typically, the observer template was often estimated from the image for which the ground truth was known *a priori*, denoted as a trainer image. Then, the estimated observer template was used to classify the image for which the ground truth was unknown, denoted as a tester image. Alternatively, it could apply a single set of the trainer image that was used to estimate the observer's template as the tester image in the FOM computation. The output FOMs of these two alternatives were optimistic as reported by Wagner et al.⁴⁴ We experimentally found that there was no significant difference ($p < 0.02$) between using the

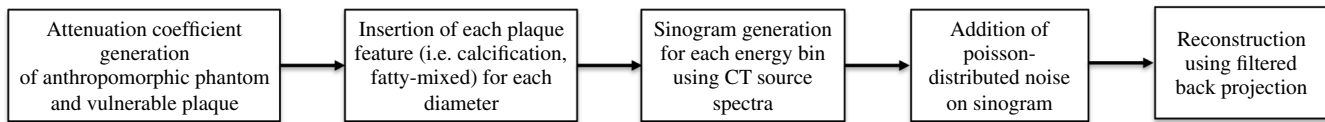


Fig. 2 Flowchart of the spectral CT image generation.

single set and a fivefold cross validation in the resulting SNRs computed by our proposed method. In this study, the same individual set of trainer and tester images was employed to estimate the observer template and the FOM computation.

2.3 Data Generation

The simulated data of a carotid atherosclerosis patient were used to validate the proposed numerical observer on the discrimination assessment framework. Figure 2 schematically shows the flowchart of the spectral CT image generation. The energy-dependent attenuation maps of the patient anatomy and vulnerable plaque in a carotid artery were generated using a digital anthropomorphic phantom. The specific plaque features were generated and then inserted into the vulnerable region in the carotid artery. Then, attenuation sinograms were created using a forward projector for fan-beam transmission tomography with realistic CT source spectra. Poisson-distributed noise was added to the sinograms, and the CT images were then reconstructed using FBP algorithms.

2.3.1 Anthropomorphic phantom

An XCAT digital phantom was used to generate spectral attenuation coefficient $\mu(E, \vec{r})$ at position \vec{r} of the patient anatomy. The attenuation maps of the anatomical background [denoted $\mu_{BG}(E, \vec{r})$] together with the attenuation maps of vulnerable plaque [denoted $\mu_{VP}(E, \vec{r})$] were generated using XCAT. Specifically, the $\mu_{VP}(E, \vec{r})$ were created by using the cardiac plaque generator available in XCAT version 2.0. The details of the chemical element compositions and densities were not specified, but the generated $\mu_{VP}(E, \vec{r})$ was realistic because the XCAT incorporated the parameterized models of humans, developed with highly detailed anatomies using nonuniform rational B-spline (NURBS) and the visible male/female anatomical datasets provided by the National Library of Medicine.⁴⁵ The carotid artery's location was selected at the origin level located in the neck above the brachiocephalic trunk of the right common carotid artery, which its average arterial diameter

was $\sim 9.1 \pm 0.2$ mm.⁴⁶ The $\mu_{VP}(E, \vec{r})$ were then inserted into the lumen of the carotid artery present in an axial slice of the generated phantom. Figures 3(a) and 3(b) show the coronal plane and the selected axial slice that has the presence of the carotid arteries in the XCAT phantom, respectively. Figure 3(c) shows an example of the attenuation map at energy 30 keV of the selected slice with a zoomed carotid lumen. The phantom pixel size of 1.03×1.03 mm² with the matrix size of 512×512 was used for these simulated data. The diameter (8-mm) of circular-shaped vulnerable plaque was inserted into the carotid lumen. This simulation was similar in that a particular vulnerable plaque was accumulated within the carotid lumen.

2.3.2 Carotid plaque features

The circular-shaped plaque features with known compositions were inserted within the vulnerable-plaque region of the carotid artery, as shown in a schematic model in Fig. 4(a). The different models of the plaque features were generated including: (1) calcified nodule (CN), (2) fatty-mixed nodule (FN), and (3) iodine-mixed blood (IB) in the vulnerable plaque.

The energy-dependent attenuation coefficients of each feature model were separately generated, regardless the generation using XCAT. According to the mixture rule of Lambert-Beer's Law, compound matter could be described as a superposition of element mass attenuation coefficients. Thus, the spectral attenuation coefficient $\mu_x(E)$ in the units of cm^{-1} was obtained as

$$\mu_x(E) = \sum_{i=1}^M P_i \left(\frac{\mu}{\rho} \right) (E, Z_i), \quad (10)$$

where the mass attenuation coefficient $(\mu/\rho)(E, Z_i)$ is a characteristic function of the i 'th element indexed by the atomic number Z_i in the periodic table of elements and P_i is the partial density or concentration in g/cm^{-3} of the i 'th element, and M is the number of elements in the compound matter.^{10,47}

For each plaque-feature model, the attenuation map was generated using Eq. (10) with the element compositions and

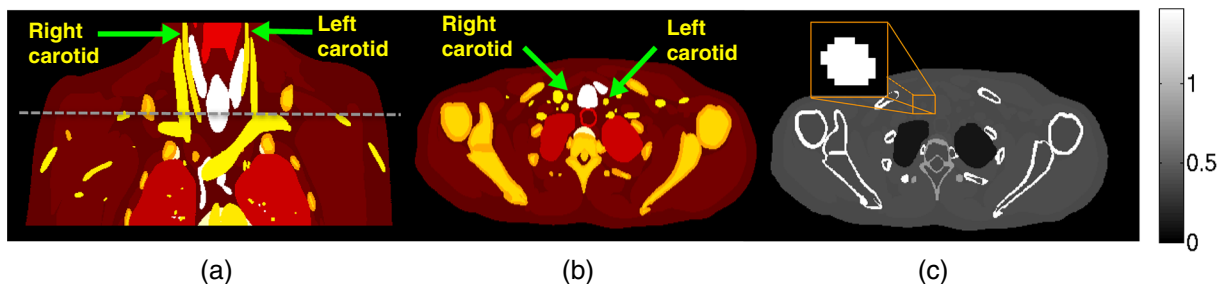


Fig. 3 An anthropomorphic torso phantom shows the right and left carotid arteries in the coronal plane. (a) The dashed horizontal line marks the location of the axial slice to be measured. (b) The selected axial slice of the anthropomorphic torso phantom shows the right and left carotid arteries, and (c) the generated attenuation map of the anthropomorphic torso phantom (cm^{-1}) displays on the selected slice at energy 30 keV. The zoomed window shows the right carotid artery.

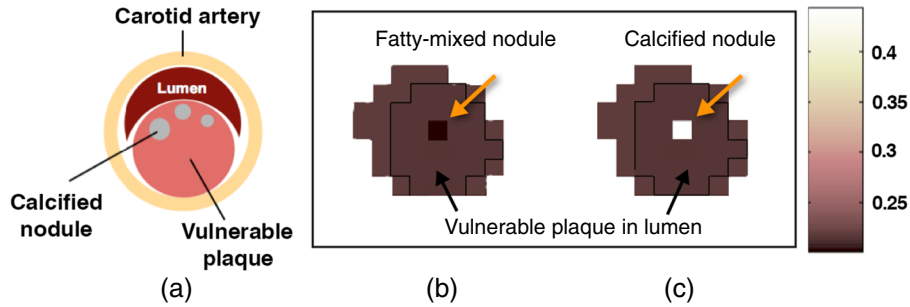


Fig. 4 (a) The schematic diagram of the carotid atherosclerosis model. The XCAT attenuation maps (cm^{-1}) at 30 keV of (b) the inserted fatty-mixed and (c) CNs in the vulnerable plaque within the right carotid artery.

Table 1 Element compositions and densities (ρ) of calcified, fatty-mixed, and iodinated-blood nodules.⁴⁸

| | | H | C | N | O | P | Cl | Ca | I | |
|-----------------------|---|---|-------|-------|-------|-------|-------|-------|--------|-----------------------------------|
| Atomic number (Z) | | 1 | 6 | 7 | 8 | 15 | 17 | 20 | 53 | ρ (g/cm^3) |
| Atomic weight (A) | | 1.01 | 12.01 | 14.01 | 16.00 | 30.97 | 35.45 | 40.08 | 126.90 | |
| Tissue substitutes | | Elemental compositions (percentage by mass) | | | | | | | | |
| 1 | Calcified nodule (CB2-50% CaCO_3) | 4.8 | 41.6 | 1.5 | 32.0 | 0.0 | 0.1 | 20.0 | 0.0 | 1.560 |
| 2 | Fatty-mixed nodule | 9.1 | 72.2 | 2.3 | 16.3 | 0.0 | 0.1 | 0.0 | 0.0 | 1.049 |
| 3 | Iodine-mixed blood | 10.2 | 11.0 | 3.3 | 74.5 | 0.1 | 0.3 | 0.0 | 20.0 | 1.060 |

densities illustrated in Table 1.⁴⁸ The energy-dependent mass attenuation coefficients, $(\mu/\rho)(E, Z_i)$, of each element were obtained from the National Institute of Standards and Technology (NIST) table.⁴⁹ Figure 4(b) and 4(c) show the attenuation maps of the inserted plaque features in the vulnerable-plaque region for FN and CN, respectively. Figure 5 depicts the generated attenuation coefficients as a function of energies for the vulnerable plaque, CN, FN, and iodinated-blood nodule.

2.4 Simulated Sinograms and Image Reconstructions

The CT measurement was simulated based upon the geometry of a GE LightSpeed CT scanner (GE Healthcare, Milwaukee, Wisconsin), which has fan-beam transmission tomography with an arc detector. The attenuation sinograms were obtained using a Fourier-based forward projector.⁵⁰ The fan-beam sinogram size was 888 samples in the angle of the ray relative to the source (σ), spaced by $\Delta\sigma \approx 0.06$ deg and 984 source positions (ξ) over 360 deg. The source-to-detector distance was ~ 949 mm. The isocenter-to-detector distance was ~ 408 mm. The quarter detector offset was also included to reduce aliasing. The effective width of the arc detector varied from 0.22 to 0.64 mm over a 40-cm field of view.

A measured projection, $p(\xi)$, having the intensity of an x-ray passed through an object with the energy dependence of the attenuation coefficient, $\mu(\xi, \eta, E)$, along the path s in the spatial coordinate, η , could be expressed as

$$p(\xi) = -\ln \left[\frac{1}{I_0} \int_{E_0}^{E_{TH}} S(E) D(E) e^{-\int_0^s \mu(\xi, \eta, E) d\eta} dE \right], \quad (11)$$

where $I_0 = \int_{E_0}^{E_{TH}} S(E) D(E) dE$ is the blank measurement, $S(E)$ is the x-ray source spectrum, and $D(E)$ is the detector response. For an ideal integrating detector, we could assume $D(E) = E$.^{47,51} Note that $(E_0, E_{TH}) \in [0, E_{\text{max}}]$ for energy

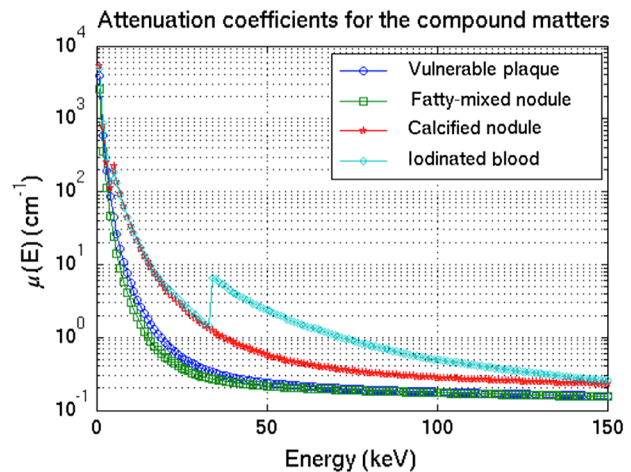


Fig. 5 The attenuation coefficient $\mu(E)$ as a function of energies for the simulated vulnerable plaque, the inserted features of CN, FN, and iodinated blood nodule. These $\mu(E)$ were generated using Lambert-Beer's law for the superposition of element mass attenuation coefficients.

integrating detectors and $(E_0, E_{TH}) \in [E_{\text{lower}}, E_{\text{upper}}]$ for MECT with the lower threshold, E_{lower} , and the upper threshold, E_{upper} , for each energy bin were assigned in the simulation.

Poisson-distributed noise was added to the generated sinograms for simulating statistical fluctuations in the measurement before the image reconstruction. The noise was generated using random numbers with a Poisson distribution with a mean parameter set to be the same as the number of photons collected by the detector in the sinograms. The noisy fan-beam sinograms were reconstructed using a conventional FBP reconstruction algorithm with Ramp or Hanning (the cut-off frequency at 0.6) filter kernels.⁵⁰ The reconstructed image pixel size was $0.98 \times 0.98 \text{ mm}^2$ with the matrix size of 512×512 . The CT images were reconstructed for each plaque feature separately, assumed that the plaque feature was perfectly decomposed from the mixture materials, so that only one plaque feature was present in the modeled region. This made the consistent scenarios in order to compare the task-based performance for all the CT systems.

2.5 CT Systems for Comparison

The discrimination assessment of plaque features was compared among various CT systems including:

1. a conventional CT system operated at 80 kVp (CT-80kVp),

2. a conventional CT system operated at 120 kVp (CT-120kVp),
3. a conventional CT system operated at 140 kVp (CT-140kVp),
4. a DECT system based on dual-source CT using 80 and 140 kVp sources (DECT-DS),
5. a DECT system based on rapid-kVp-switching CT using 80 and 140 kVp sources (DECT-SW), and
6. an MECT system based on photon-counting detectors with a source operated at 120 kVp (MECT-PC).

For all the CT systems, the source spectra were generated using SPEKTR.⁵² Figure 6 and Table 2 illustrate the probability density function (PDF) of photon flux as a function of energy (keV) and the details of the x-ray spectra for each CT system, respectively. As illustrated, the lower energy spectrum mainly consisted of Bremsstrahlung while the higher energy spectrum included the characteristic lines of the tungsten anode. For all the investigated modalities, the source spectra were normalized to deliver the same amount of dose to the patient phantom. The total entrance skin exposures applied to the phantom for all the CT systems were the same with x-ray exposure of 20 mR entrance skin per projection. With the same phantom and the same detector geometry used, the same amount of dose was

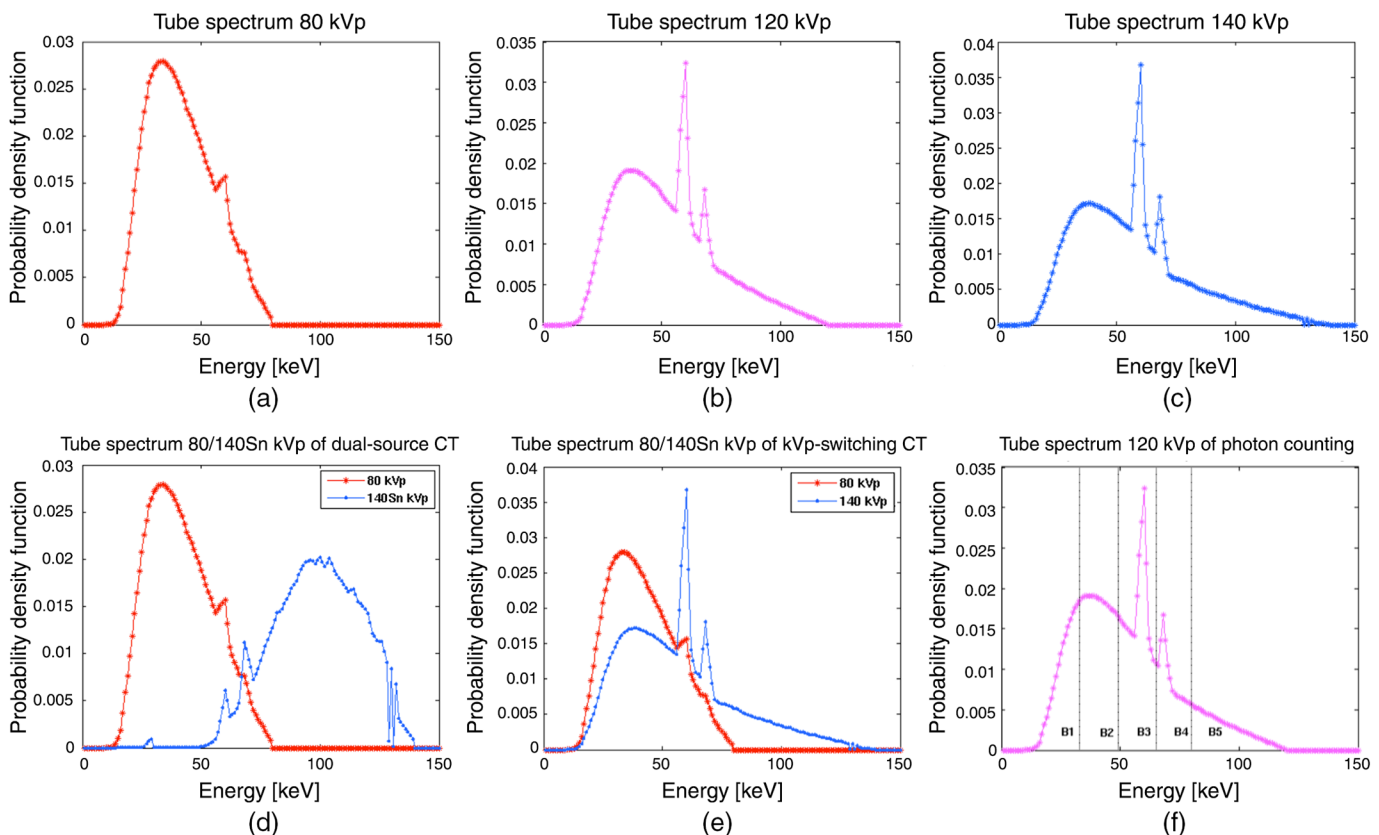


Fig. 6 The PDF of photon flux as a function of energy (keV) of X-ray spectra generated by SPEKTR: (a) the tube spectrum of CT-80kVp, (b) the tube spectrum of CT-120kVp, (c) the tube spectrum of CT-140kVp, (d) the tube spectra of DECT-DS, (e) the tube spectra of DECT-SW, and (f) the tube spectrum of MECT-PC systems. Vertical dashed lines in (f) represent energy bin thresholds assigned as 33, 49, 65, 80, and 120 keV.

Table 2 SPEKTR Tube spectrum information.⁵²

| Tube spectrum | Exposure (mR/mAs at SAD) ^a | Fluence/exposure (x-rays/mR/mm ²) | Mean energy (keV) |
|---------------------------|---|--|----------------------|
| 80 kVp | 9.70 | 193,578 | 41.80 |
| 120 kVp | 19.12 | 224,812 | 52.51 |
| 140 kVp | 24.37 | 229,793 | 56.47 |
| 140 kVp with Sn 1.0 mm | 1.00 | 237,155 | 98.14 |

^amR = milli-roentgen (described x-ray exposure), mAs = milli-ampere · seconds (described tube current), SAD is the distance from the fan-beam vertex to the center of rotation.

matched for all CT systems.⁵³ In practice, this was equivalent to adjust the tube current (mAs) to deliver the same total amount of x-ray quanta. In the simulation, there were 10^4 to 10^6 quanta for an I_0 measurement.

For DECT-DS, the additional tin (Sn) filtration of 1.0 mm at 140 kV was applied to increase the spectral separation between the low- and the high-energy spectra as well as narrowing the 140-kV spectrum.^{8,54} For both DECT-DS and DECT-SW, the x-ray exposure from both tubes matched that of a single-source CT protocol, with the dose ratio of the low- and high-energy spectra was 19:1. By performing the experiment, this ratio was chosen empirically to maximize the discrimination performance of DECT. By testing with several ratios, the 19:1 ratio maximized the discrimination performance of DECT. This is due to the fact that the lower energy photons carry larger contrast between different tissues than higher energy photons,⁹ so a larger fraction was given to the low-kVp source rather than the high-kVp source. The MECT-PC system separated detected photons into five different energy bins with upper thresholds at 33, 49, 65, 80, and 120 keV, which were selected to exploit the K-edge of iodine while the rest of the energy thresholds chosen for a nearly equal number of counts contained in each bin, following the work by Baturin et al.⁴ The mean energies of the kV spectra were 41.80, 52.51, 56.47, 41.80(98.14), 41.80(52.51), and 52.51 keV for CT-80kVp, CT-120kVp, CT-140kVp, DECT-DS, DECT-SW, and MECT-PC, respectively. For all the CT systems, projection data were simulated with energy-weighted integrals over 1 keV spectral steps. For MECT-PC, the multienergy sinograms were acquired and reconstructed for each energy bin. Although data acquired at each energy (either within a bin of photon-counting detectors or at a single tube-voltage setting) were treated as independent measurements, a high degree of correlation among these energy-specific datasets was achieved due to the exact same patient anatomy was measured in each case.³³ Two independent measurements with and without the object (blank scans) were acquired for each CT method for a population of 50 noise realizations. By performing the experiment with 250 noise realizations, we determined that 50 noise realizations provided a stable covariance estimation of the templates used in our two-staged numerical observer. As it is ideal, the simulation and analyses were performed on an ensemble of the reconstructed images from the same phantom under identical scan conditions, in order to remove the impact of the correlated nature of the CT image noise as well as to remove the potential

biases due to image artifacts resulting from the imperfect system calibration.⁵⁵

To demonstrate the method, several assumptions were made for the CT systems in the observer performance comparison. For all the CT systems, the detector response was assumed to provide 100% of quantum detection efficiency. For DECT-SW, the actual tube voltage was assumed to yield the ideal rectangular switching curve. As a result, there was no overlapping of data acquisition from the under- and overshoot of the x-ray tube voltage during switching processes. For MECT-PC, the photon counting detectors were assumed to have perfect energy resolution with no charge sharing and pulse pile-up effects, thereby no distortions to detected spectrum.

2.6 Performance Evaluation

The observer performance was evaluated for two discrimination tasks: (1) calcified plaque versus fatty-mixed plaque (DT-1) and (2) iodinated blood versus calcified plaque (DT-2) on the reconstructed images, using FBP with Ramp and Hanning kernels. In these defined tasks, the first scenario was equivalent to the identification task for calcified plaque in noncontrast imaging. The second scenario was equivalent to the identification task for calcified plaque when using iodinated contrast agent. However, the discrimination task for fatty-mixed plaque and iodinated blood was not included in this study because it is known in the CT community that it is not difficult to distinguish these two materials in spectral CT (both in DECT and MECT).^{8,56} The indistinguishability of these two materials can occur in conventional CT, and we, here, focus on spectral CT performance, rather than the performance of conventional CT.

Feature-to-vulnerable-background contrasts (C_F) for CN, FN, and iodinated-blood nodule were calculated. First, the region of interest (ROI) of an 11×11 window centered on each plaque feature was defined in the reconstructed CT image. This ROI was then divided into two subregions: a 4×4 ROI centered on the plaque feature (denoted ROI_{PF}) and a surrounding 7×7 ROI shell (denoted ROI_{VPB}), treated as the vulnerable-plaque background for that particular plaque feature. The contrast metric was computed as the average over N_R , where N_R is the number of noise realizations

$$C_F = \frac{1}{N_R} \sum_{r=1}^{N_R} \hat{C}_F^r, \quad (12)$$

where $\hat{C}_F^r = \frac{\text{avg}(\text{ROI}_{\text{PF}}^r)}{\text{avg}(\text{ROI}_{\text{VPB}}^r)}$, for each noise realization r . Note that $\text{avg}(\text{ROI}_x^r) = \frac{1}{Q} \sum_{i \in \text{ROI}_x^r} \gamma_i^r$ is the average intensity value of the total number of Q pixels inside the ROI for noise realization r . Feature contrast ratios (CR_F) of the images—defined as a contrast ratio of the material-paired combinations described in the identification task of DT-1 and DT-2—were computed.

The appropriate numerical observers were selected to match with the dimensionality of the investigated images. For CT-80kVp, CT-120kVp, and CT-140kVp, the observer evaluation was performed using a conventional 2-D CHO model with 5-LG channels. For DECT-DS and DECT-SW, the proposed numerical observer with two energy bins ($J = 2$) was used and one with five energy bins ($J = 5$) was used for MECT-PC. The ROI of a 31×31 window centered on a target plaque feature for a pair of investigated materials were input to a numerical

observer. The different window size of the investigated material did not alter the FOM results. For MECT and DECT, the same 5-LG channels were used for all the energy windows. To be optimal at all signal diameters, the spread parameter $d_u = 3$ was empirically chosen and applied to all numerical observers used in this study. The material identification was performed on the given plaque features for the discrimination tasks of DT-1 and DT-2. For all the CT methods, the plaque discrimination was evaluated for:

- Performance comparison of discrimination task on SKE/BKE: the diameter of the signal (ϕ) was constant at 1.8 mm, referred to constant plaque density or concentration.
- Performance comparison of discrimination task on SKS/BKE: the diameter of the signal was increased as a Gaussian-distributed function, $\phi \in [2.3, 7.1]$ mm, referred to changes of plaque density or concentration. Note that the diameter of 1.8-mm plaque was not included here because this task was already performed in the previous experiment. In principle, the SKS task is the extended paradigm of the SKE, in which the observer performs multiple SKE tasks with varying target diameters.

The FOMs of SNR and AUC for the two discrimination tasks of DT-1 and DT-2 were computed using Eqs. (8) and (9). The discriminated SNR per a unit of dose (SNR_{DIS}) was computed as

$$\text{SNR}_{\text{DIS}} = \text{SNR}/\sqrt{D}, \quad (13)$$

where D is the total skin exposure.^{4,51}

For SKS/BKE, according to the outcome AUC range in Eq. (9) was limited by the Gaussian error function, the SNRs first obtained using Eq. (8) of all the varying signals and for all the CT systems were converted to a certain range that approximately fitted the criterion of AUC, covering the range from 0.5 to 1.0, prior input to Eq. (9). With this conversion, it improved the analysis investigation of the performance comparison for all the investigated CT systems.

3 Results

3.1 Simulation Results

The plaque-feature discrimination tasks were performed on simulated images reconstructed for different CT systems (i.e., CT-80kVp, CT-120kVp, CT-140kVp, DECT-DS, DECT-SW, and MECT-PC) and different reconstruction parameters (i.e., FBP-Ramp and FBP-Hanning), as shown in Fig. 7. As expected, the reconstructed images using FBP-Ramp were noisier than those reconstructed using FBP-Hanning for all CT systems. For both the reconstructed parameters, the image intensities of the lower energy spectra (or energy bins for MECT) were brighter than those of the higher energy spectra, when comparing within the same type of the acquisition method (i.e., among three conventional CTs or between the low- and high-energy kVp for DECT or among energy bins for MECT). As expected, more beam hardening artifacts in the form of shading and streaking artifacts were found at lower energy bins.

Table 3 shows C_F for the CN, FN, and IB features obtained using both FBP-Ramp and FBP-Hanning. FBP-Ramp yielded similar C_F means as FBP-Hanning for all features. However,

the standard deviations (std) of C_F appeared higher for FBP-Ramp as compared to FBP-Hanning. For the conventional CT simulations, CT-80kVp yielded higher C_F than both CT-120kVp and CT-140kVp for the CN and IB features. Similar results were also observed in MECT-PC, as the lower energy bins yielded higher C_F than the higher energy bins. These results were consistent with the previous study performed by Saba et al.²⁸ However, we did not see this characteristic for the FN feature, as the $C_{F\text{-FN}}$ for all energy spectra for the CT systems were not very different. Energy bins $j = 2$ of DT-2 were the highest as compared to other energy bins for MECT-PC in both reconstructed images.

For FBP-Ramp and FBP-Hanning images, Figs. 8 and 9 show the boxplots of CR_F , the ratios of the feature contrasts for calcified plaque versus fatty-mixed plaque ($C_{F\text{-CN}}/C_{F\text{-FN}}$) and iodinated blood versus calcified plaque ($C_{F\text{-IB}}/C_{F\text{-CN}}$) at the diameter of 1.8 mm for DT-1 and DT-2. CR_F means were similar while CR_F stds were higher for FBP-Ramp as compared to FBP-Hanning for both DT-1 and DT-2 and for all CT systems. CR_F of DT-2 yielded higher CR_F than DT-1, as observed in both FBP-Ramp and FBP-Hanning. Similar to Table 3, we observed that CR_F of lower energy spectra yielded higher than those of the higher energy spectra, as compared among the different conventional CTs and that among different energy bins of MECT-PC, respectively. Interestingly, this observation did not appear for DT-2 for MECT-PC, as energy bin $j = 1$ and $j = 2$ yielded relatively low and high values, respectively, both in FBP-Ramp and FBP-Hanning.

3.2 Performance Comparison of Discrimination Task on Signal-Known-Exactly and Background-Known-Exactly

The discrimination SNRs of the plaque material identification tasks were compared among the different investigated CT systems and different reconstruction parameters, as shown in Figs. 10(a) and 10(b) for DT-1 and DT2, respectively. As shown in Fig. 10(a), the overall discrimination SNRs of all CT systems for DT-1 was inferior to the overall performance of DT-2 shown in Fig. 10(b) by 32.9% and 34.7% for FBP-Ramp and FBP-Hanning, respectively. The FBP-Hanning images provided a higher discrimination performance than the FBP-Hanning images for all CT acquisition methods. Superior discrimination performance was achieved using MECT-PC over the DECT (-DS, -SW) and conventional CT (80kVp, 120kVp, 140kVp) methods for DT-1 ($p < 0.002$ and $p < 0.003$ for FBP-Ramp and FBP-Hanning, respectively) and for DT-2 ($p < 0.002$ and $p < 0.006$ for FBP-Ramp and FBP-Hanning, respectively). Among the three conventional CTs, the discrimination SNRs decreased as tube voltages increased. For both tasks, the observer performances of the DECT systems outperformed that of the conventional CTs. However, the discrimination SNRs using FBP-Hanning images of both DECT systems were not as good as that of CT-80kVp for DT-2. By comparing the two DECT systems, we could not conclude which system performed better. The findings indicated that the MECT system yielded superior performance over other CT systems for the identification tasks of calcified plaque, fatty-mixed plaque, and iodinated-mixed blood as compared at equivalent dose.

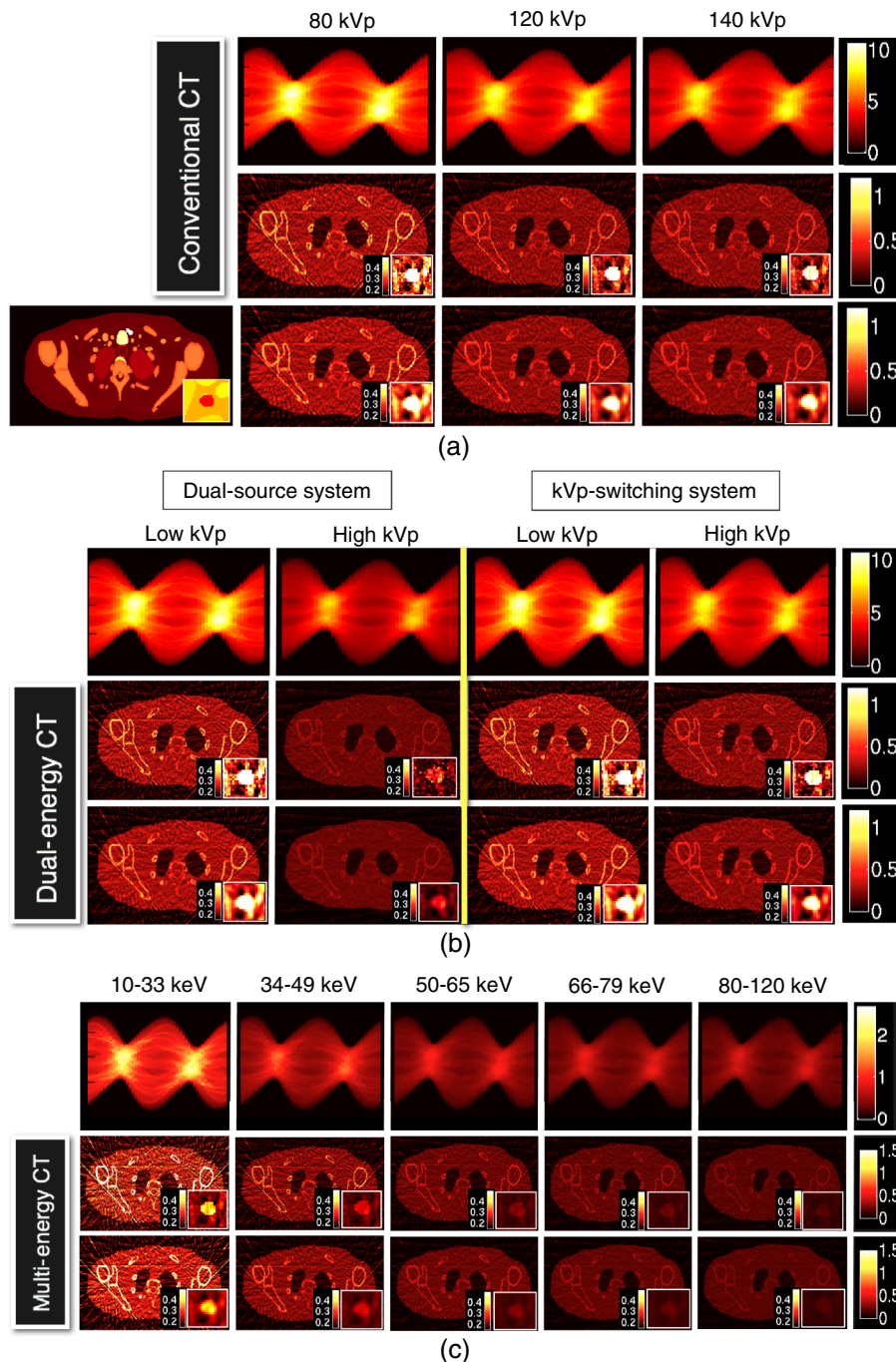


Fig. 7 The generated fan-beam sinograms and reconstructed images using the FBP reconstruction method for Ramp [the middle rows of (a), (b), and (c)] and Hanning filters [the bottom rows of (a), (b), and (c)]: (a) the conventional CT with 80, 120, and 140 kVp (denoted CT-80kVp, CT-120kVp, and CT-140kVp, respectively); (b) the DECT of dual-source CT (denoted DECT-DS) and rapid kVp switching CT (denoted DECT-SW); and (c) the MECT using photon-counting detector (denoted MECT-PC). The carotid calcified plaque of 8-mm diameter is displayed at the bottom right corner of each image. The ground truth image (XCAT) is displayed at the lower left in (a).

3.3 Performance Comparison of Discrimination Task on Signal-Known-Statistically and Background-Known-Exactly

The effect of mass thicknesses or diameters of Gaussian-shaped inserted plaque features were investigated in the identification tasks of DT-1 and DT-2 on the tested CT systems. All

discrimination AUCs of all varied signals for DT-1 and DT-2 were computed for both reconstruction parameters. Figure 11 shows the plots of AUC as a function of signal certainty (defined as the varied diameters as a Gaussian distribution of the plaque features) for the plaque discrimination task using different CT systems and different reconstruction parameters. The AUC values were fitted using polynomial functions and the results were

Table 3 The feature-to-vulnerable-background contrasts (C_F) for CN, FN, and iodinated-blood nodule of the investigated CT systems with FBP-Ramp and FBP-Hanning.

| CT System | Feature-to-vulnerable-background contrast (C_F) ^a | | | | | |
|---------------|--|---------------------|-------------------------|---------------------|-----------------------------|---------------------|
| | Calcified nodule (CN) | | Fatty-mixed nodule (FN) | | Iodinated-blood nodule (IB) | |
| | FBP-Ramp | FBP-Hanning | FBP-Ramp | FBP-Hanning | FBP-Ramp | FBP-Hanning |
| CT-80kVp | $1.3e+0 \pm 1.0e-2$ | $1.3e+0 \pm 0.5e-2$ | $9.8e-1 \pm 9.4e-3$ | $1.0e+0 \pm 0.4e+2$ | $2.3e+0 \pm 1.3e-2$ | $2.2e+0 \pm 0.6e-2$ |
| CT-120kVp | $1.2e+0 \pm 1.3e-2$ | $1.2e+0 \pm 0.5e-2$ | $1.0e+0 \pm 1.2e-2$ | $1.0e+0 \pm 0.5e-2$ | $2.0e+0 \pm 1.3e-2$ | $1.9e+0 \pm 0.5e-2$ |
| CT-140kVp | $1.2e+0 \pm 1.1e-2$ | $1.2e+0 \pm 0.5e-2$ | $1.0e+0 \pm 1.2e-2$ | $1.0e+0 \pm 0.4e-2$ | $1.9e+0 \pm 1.4e-2$ | $1.9e+0 \pm 0.5e-2$ |
| DECT-DS $j=1$ | $1.3e+0 \pm 1.0e-2$ | $1.3e+0 \pm 0.5e-2$ | $9.8e-1 \pm 1.2e-2$ | $1.0e+0 \pm 0.5e-2$ | $2.3e+0 \pm 1.3e-2$ | $2.2e+0 \pm 0.7e-2$ |
| DECT-DS $j=2$ | $1.8e+0 \pm 4.5e-2$ | $1.8e+0 \pm 2.0e-2$ | $1.3e+0 \pm 3.5e-2$ | $1.0e+0 \pm 1.6e-2$ | $3.1e+0 \pm 6.1e-2$ | $3.1e+0 \pm 2.8e-2$ |
| DECT-SW $j=1$ | $1.3e+0 \pm 1.0e-2$ | $1.3e+0 \pm 0.5e-2$ | $9.8e-1 \pm 1.2e-2$ | $1.0e+0 \pm 0.5e-2$ | $2.3e+0 \pm 1.3e-2$ | $2.2e+0 \pm 0.7e-2$ |
| DECT-SW $j=2$ | $1.5e+0 \pm 3.0e-2$ | $1.5e+0 \pm 1.4e-2$ | $1.1e+0 \pm 2.7e-2$ | $1.1e+0 \pm 1.1e-2$ | $2.6e+0 \pm 6.1e-2$ | $2.6e+0 \pm 1.9e-2$ |
| MECT-PC $j=1$ | $1.6e+0 \pm 2.4e-2$ | $1.6e+0 \pm 1.1e-2$ | $9.0e-1 \pm 1.8e-2$ | $1.0e+0 \pm 0.9e-2$ | $1.6e+0 \pm 1.9e-2$ | $1.7e+0 \pm 0.8e-2$ |
| MECT-PC $j=2$ | $1.3e+0 \pm 1.8e-2$ | $1.3e+0 \pm 0.8e-2$ | $9.6e-1 \pm 1.6e-2$ | $1.0e+0 \pm 0.8e-2$ | $3.1e+0 \pm 2.7e-2$ | $3.0e+0 \pm 1.3e-2$ |
| MECT-PC $j=3$ | $1.2e+0 \pm 2.1e-2$ | $1.2e+0 \pm 0.9e-2$ | $1.0e+0 \pm 1.9e-2$ | $1.0e+0 \pm 0.7e-2$ | $1.9e+0 \pm 2.2e-2$ | $1.9e+0 \pm 1.0e-2$ |
| MECT-PC $j=4$ | $1.1e+0 \pm 3.0e-2$ | $1.1e+0 \pm 1.1e-2$ | $1.0e+0 \pm 3.6e-2$ | $1.0e+0 \pm 1.3e-2$ | $1.6e+0 \pm 3.5e-2$ | $1.6e+0 \pm 1.6e-2$ |
| MECT-PC $j=5$ | $1.0e+0 \pm 3.1e-2$ | $1.1e+0 \pm 1.3e-2$ | $1.0e+0 \pm 3.1e-2$ | $1.0e+0 \pm 1.3e-2$ | $1.3e+0 \pm 3.0e-2$ | $1.3e+0 \pm 1.4e-2$ |

^aEach C_F was in the format as mean \pm standard deviation (std), where std was computed over the contrasts of 50 noise realizations.

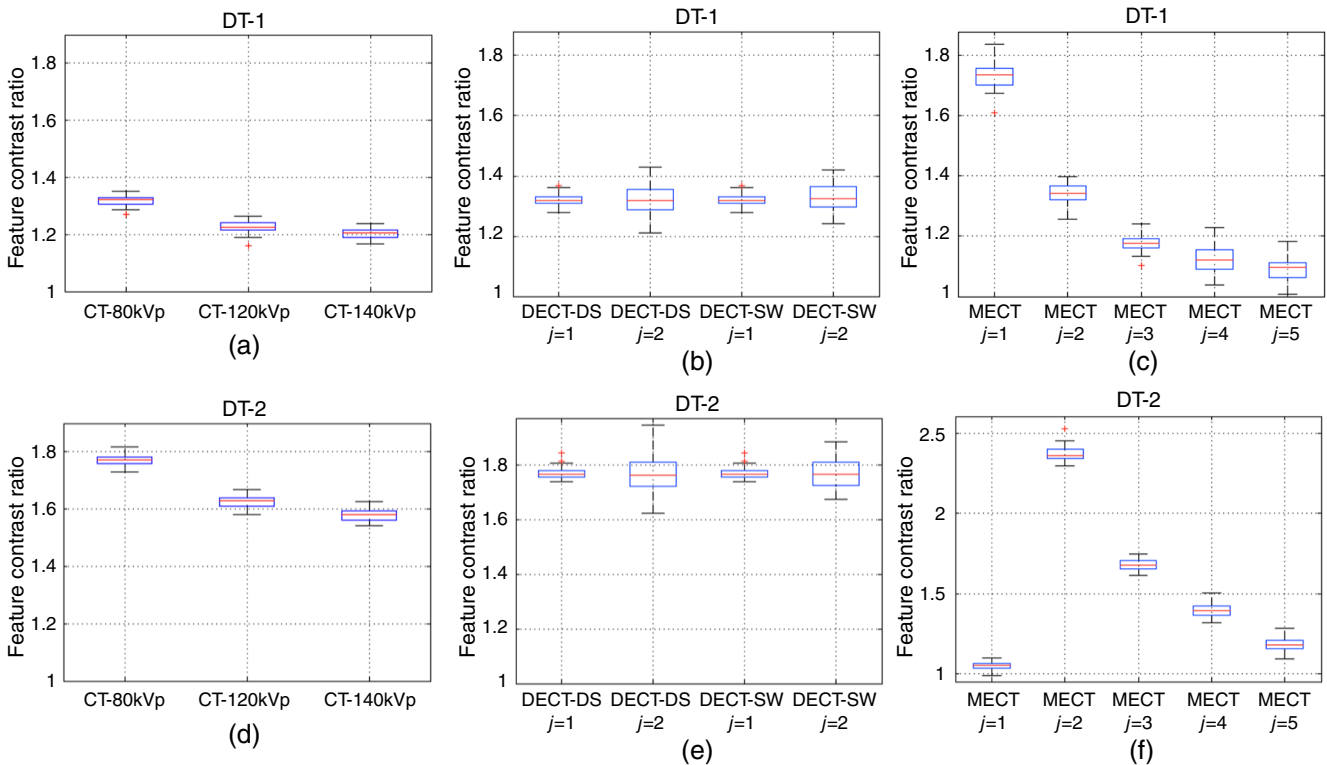


Fig. 8 The boxplots illustrate the feature contrast ratios (CR_F) for the identification task of calcified plaque vs. fatty-mixed plaque (DT-1) and the identification task of iodinated blood vs. calcified plaque (DT-2) using FBP-Ramp images for: (a,d) conventional CT (CT-80kVp, CT-120kVp, and CT-140kVp), (b, e) DECT (DECT-DS and DECT-SW), and (c,f) MECT (MECT-PC).

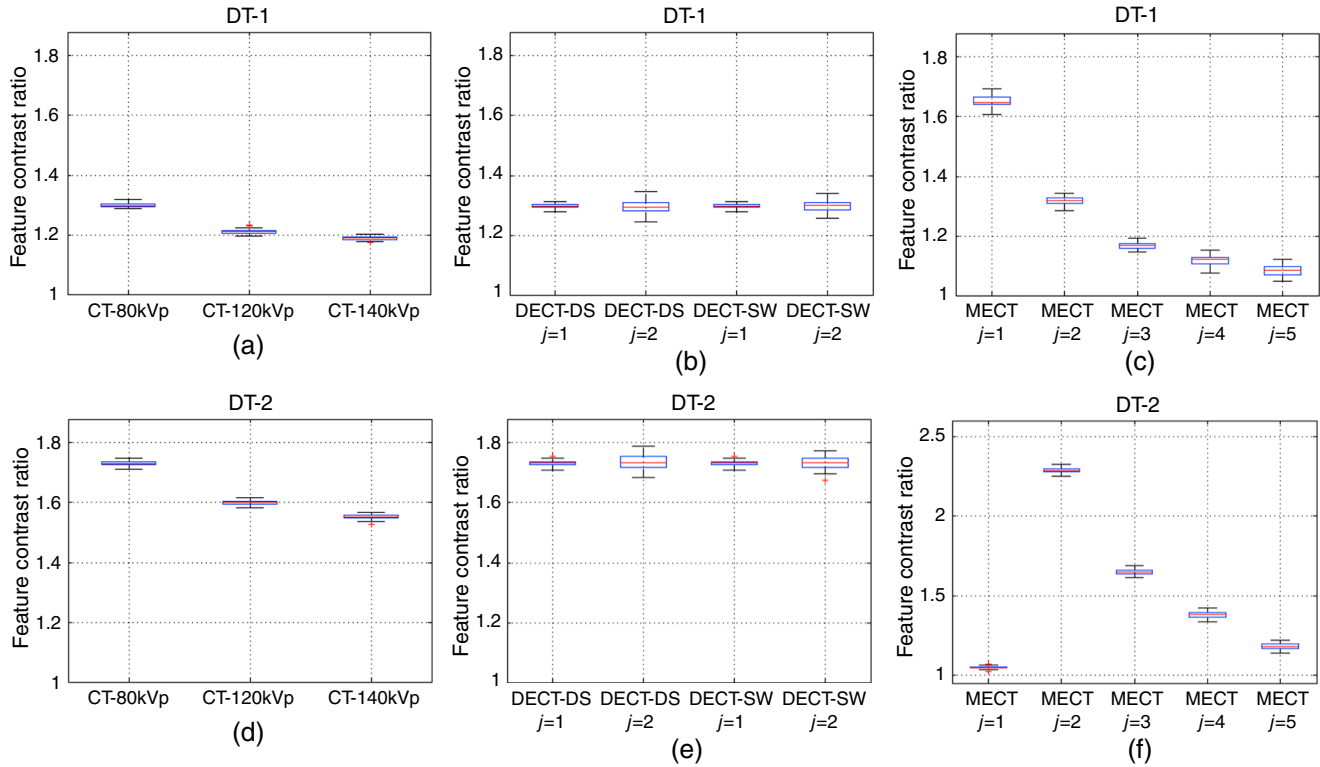


Fig. 9 The boxplots illustrate the feature contrast ratios (CR_F) for the identification tasks of DT-1 and DT-2 using FBP-Hanning images for: (a,d) conventional CT (CT-80kVp, CT-120kVp, and CT-140kVp), (b,e) DECT (DECT-DS and DECT-SW), and (c,f) MECT (MECT-PC).

plotted. For all the investigated CT systems, the observer performance increased as the increased signal certainty, whereas MECT-PC yielded the highest performance at all levels of the signal certainties as illustrated in both reconstruction

parameters. By comparing among the conventional CTs, the higher energy-spectrum CTs (CT-120kVp, CT-140kVp) yielded almost the least performance, whereas CT-80kVp and the DECT systems (DECT-DS, DECT-SW) provided comparable performance.

Figures 11(a) and 11(c) show the discrimination AUCs for the identification tasks of DT-1 and DT-2 with the FBP-Ramp algorithm, while Figs. 11(b) and 11(d) show results for FBP-Hanning of DT-1 and DT-2, respectively. As expected, FBP-Ramp reconstructed images provided inferior discrimination performance than the FBP-Hanning reconstructed images for all signal levels. With the different identification tasks, the overall AUCs of all CT systems for DT-2 were higher than those for DT-1, for both FBP-Ramp and FBP-Hanning. These results demonstrated that the MECT system outperformed other methods in discriminating carotid plaque features for all levels of signal uncertainties and reconstructed methods.

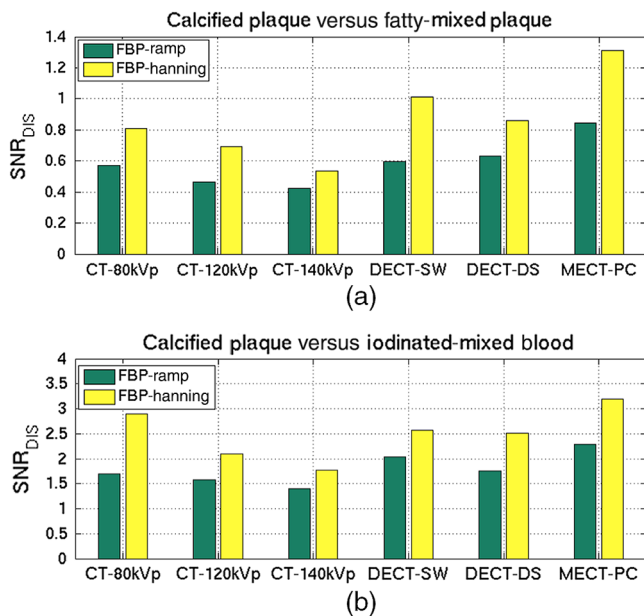


Fig. 10 The discrimination SNR results per an effective dose for (a) the identification task of DT-1 and (b) the identification task of DT-2 as compared for CT-80kVp, CT-120kVp, CT-140kVp, DECT-DS, DECT-SW, and MECT-PC using the FBP reconstructed algorithm with Ramp and Hanning filters.

4 Discussion

In this study, a numerical observer incorporated multiple spectral energies and a material-discrimination framework for spectral CT assessment were proposed and evaluated. The binary-discrimination tasks of the SKE/BKE framework and the signal variability based on the SKS/BKE framework were performed in classifying the carotid-plaque features. Significant improvements in terms of observer performance for MECT were achieved as compared to DECT and conventional CT systems at an equivalent dose level.

It is clear that MECT-PC provides superior performance over the other acquisition methods for all cases. On average of signal variability, MECT-PC outperformed DECT-DS, DECT-SW, CT-

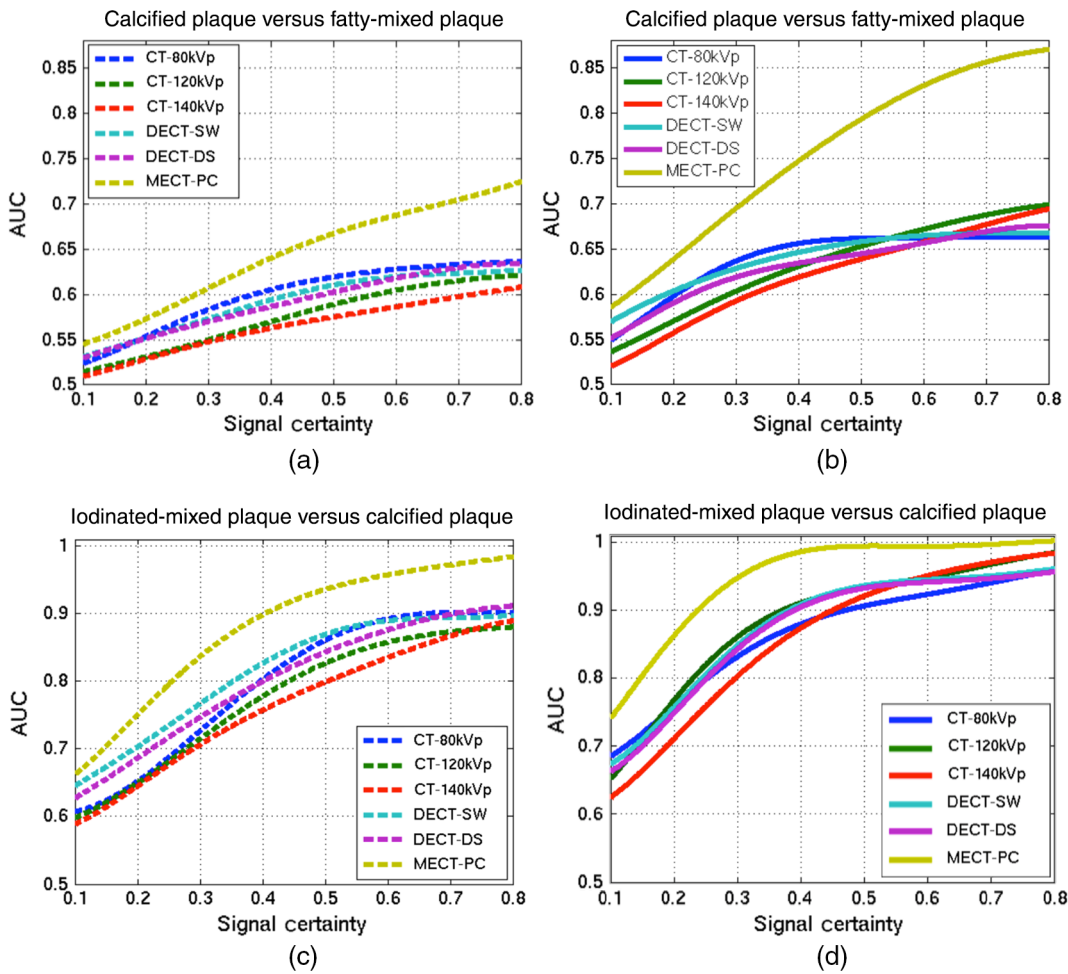


Fig. 11 The area under the receiver operating characteristic curve (AUC) as a function of signal certainty for (a,b) the identification task of DT-1 using FBP-Ramp and FBP-Hanning, respectively; and (c,d) the identification task of DT-2 using FBP with Ramp and Hanning, respectively, acquired using the CT-80kVp, CT-120kVp, CT-140kVp, DECT-DS, DECT-SW, and MECT-PC systems. Note that the *dashed lines* referred to using FBP with the Ramp filter and the *solid lines* referred to using FBP with the Hanning filter.

80kVp, CT-120kVp, and CT-140kVp, as the SNR improvements of the classification tasks were in the range of 46.8% to 65.3% (all $p < 0.01$) for FBP-Ramp images and 53.2% to 67.7% (all $p < 0.01$) for FBP-Hanning images in both identification tasks. The SNR improvements of MECT-PC as compared to the other modalities were calculated as illustrated in Table 4. As illustrated in Table 4, the overall improvements of FBP-Ramp were higher than those of FBP-Hanning for both identification tasks. This implies that MECT-PC can be used to improve material-discrimination performance when a reconstruction method is chosen.

The proposed numerical observer appropriately accounts for both signal and noise appearing in images. In this study, the noise is attributable to the measurement process (Poisson-distributed noise) and also that appeared in reconstructed images, which is pertinent to the reconstruction process. Specifically, the different noise levels using the different reconstruction parameters constitute important evidence to demonstrate that our numerical observer properly correlates the image noise that occurred in each energy bin and across different energy bins

Table 4 The improvement of the discrimination performance of MECT-PC as compared to other investigated CT systems on the average of signal variability.

| No. | CT system | SNR improvement of MECT-PC (%) | | | |
|-----|-----------|--------------------------------|-------------|----------|-------------|
| | | DT-1 | | DT-2 | |
| | | FBP-Ramp | FBP-Hanning | FBP-Ramp | FBP-Hanning |
| 1. | CT-80kVp | 65.3 | 47.8 | 63.8 | 53.2 |
| 2. | CT-120kVp | 55.8 | 48.7 | 59.0 | 59.9 |
| 3. | CT-140kVp | 51.2 | 47.0 | 55.8 | 57.9 |
| 4. | DECT-DS | 62.1 | 46.8 | 64.8 | 54.0 |
| 5. | DECT-SW | 64.1 | 48.5 | 67.7 | 54.8 |

of MECT-PC (or different voltage spectra of DECT) in the FOM computation. As expected, the overall SNR of FBP-Ramp images is inferior to that of FBP-Hanning images for all cases. These indicate that our numerical observer can be used to appropriately assess and compare the overall diagnostic values of material discrimination in different CT systems and reconstructions.

The reconstructed images using the FBP algorithm with Ramp filters have poorer noise performance than those with Hanning filters. Typically, the Ramp-filtered kernel preserves high-frequency contents (i.e., edges) in the projection data while it also enhances image noise, with most noise presenting itself as high-frequency features. Using the FBP algorithm, the choice of the filter kernel represents a trade-off between noise and spatial resolution. The spatial resolution of CT systems can be quantified using the impact of the modulation transfer function (defined as the ratio of the output modulation to the input modulation), which is useful for measuring a system response to different frequencies. Typically, a high-resolution reconstruction kernel yields an increased noise level. Hence, for each clinical application, an appropriate choice of the filter kernel is specifically chosen to balance these two factors. For example, the GE LightSpeed CT scanner has six different types of filters: soft, standard, detail, lung, bone, and edge,⁵⁵ which the bone kernel is often used to examine fine structures but providing noisier images. With an increased inherent spatial resolution, the later scanner Discovery CT750 HD (GE Healthcare; Milwaukee, Wisconsin) provides an additional five reconstruction kernels to optimize the appearance of stent, calcified plaques, soft plaques, or stenosis for cardiac imaging.⁵⁵ Unfortunately, the design details of these filters are commonly considered proprietary and are inaccessible in the public domain.

For the conventional CTs, it is not surprising that CT-80kVp has the highest discrimination performance as compared to CT-120kVp and CT-140kVp. With an increasing tube voltage, the efficiency of the x-ray tube as well as the penetration of the radiation is increased. As a result, there is larger penetration of the radiation and it causes the image contrast to decrease.⁵¹ This can be shown in terms of the attenuation coefficient characteristics illustrated in Fig. 5. As shown, the attenuation differences between the higher atomic number (Z) plaque materials (i.e., iodine and calcium) and the lower Z plaque material (i.e., mixed fat) become smaller at higher energy levels. The plaque composition with higher Z material, such as iodine ($Z = 53$, density = 4.93 g/cm^3) or calcium ($Z = 20$, density = 1.55 g/cm^3), usually attenuates more radiation. Hence, both the elevated density and the calcium/iodine mass contributions lead to a comparably strong x-ray attenuation of calcified/iodinated materials, especially in particular for low energies, yielding high attenuation values. This attenuation is most pronounced for the photoelectric effect owing to these materials' high effective atomic number. By contrast, the composition with lower Z material, such as soft tissue or fat (effective $Z = 10$, density = 1 g/cm^3), shows a smaller effect and yields low attenuation values due to Compton scattering dominance.^{29,30} At increasing tube voltages, the material discrimination performance decreases according to the material contrast decreases.

Using the DECT systems, even though they have additional characteristic information from the high-kVp sources, they seem to not provide great benefit. The additional high-kVp information is unlikely to significantly enhance the detail of the material characteristics. As can be seen in Figs. 8(b) and

8(e) and Figs. 9(b) and 9(e), the CR_F values of the low- and high-kVp are almost similar. This implies the similar characteristics using the low- and high-tube voltages. The higher noise of the high-kVp sources of DECT is caused by the contribution of fewer photon counts due to the dose domination setup, as the fraction of the highkVp source spectrum is quite small (1:19). Hence, the lower-energy spectrum of DECT used almost the same tube current as applying to the single source of the conventional CT systems. As a result, the influence of low-kVp mainly dominates to the signals, and the DECT systems show similar performances to the conventional CT systems, especially CT-80kVp. In addition, increasing the dose fraction for high-kVps does not improve the SNRs, as we have tested in the experiment. Interestingly, the discrimination SNRs of DECT are sometimes worse than of the single-source CT with 80kVp, as shown in DT-2 using FBP-Hanning in the SKE/BKE framework (see Fig. 10). Like the SKE/BKE task, the signal-variation study (SKS/BKE) sometimes shows inconsistency of the discrimination performances among the DECT (-DS, -SW) systems and the conventional CT systems, especially CT-80kVp. These findings are similar to the recent comparison studies showing that dual-energy acquisitions can provide similar or even improved contrast-to-noise ratios at an equivalent dose.^{57,58} This indicates that additional material characteristics obtained using DECT may not reliably improve the ability to differentiate various material compositions in plaque imaging.

MECT-PC provides substantial differentiation because it makes use of additional specific characteristics obtained from the energy discrimination capability of photon-counting detectors. Unlike the CT systems that are equipped with integrating detectors, photon-counting detectors separate the energy deposits of each photon interacting with the detector, thereby providing better classification performance. The conventional CTs and some designs of DECT systems integrate the charge generated by x-ray photon interactions in the detector, so they provide non-specific energy information regarding individual photons. In principle, the overlap of the weighting functions between the narrowly separated energy bins can be eliminated using an ideal energy-resolving counting detector. Hence, images using photon-counting detectors can reduce relative errors (uncertainty) in material decomposition.³³ As demonstrated in our study, MECT-PC has improved the FOM over other CT systems. Similar to DECT, the low-energy bins of MECT-PC mainly contribute to the SNR. Typically, the material characteristics between the spotty calcification and the iodine contrast agents can be readily separated, as the information obtained in each energy bin shows very different characteristics, especially in energy bin $j = 1$ and $j = 2$ for the identification tasks of DT-1 and DT-2 [see Figs. 8(c) and 8(f) and 9(c) and 9(f)]. The large contrast at energy bin $j = 2$ of DT-2 contains the K -edge energy information of iodine (33.2 keV), illustrating the different characteristics of this material. Figure 12 can be used to confirm the specific attenuation characteristics of the plaque features within the ROIs from the five energy bins of MECT-PC. As shown, the energy bin $j = 2$ contains the peak of the iodine attenuation coefficients. This demonstrates that the proposed numerical observer locally processes the information (i.e., signal, noise) from each energy bin and provides a proper integration of this information across the multiple energy bins.

Our numerical observer appropriately incorporates both the spatial information of each energy-specific image within each

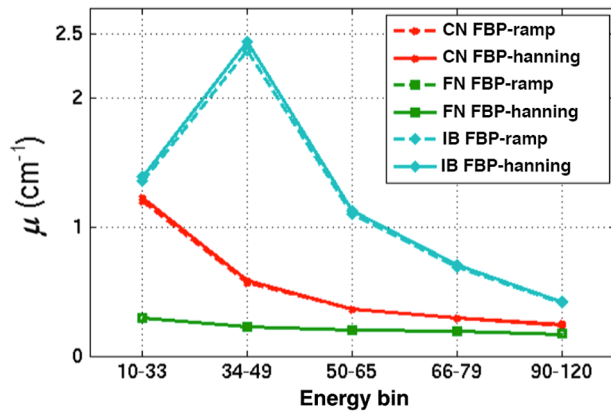


Fig. 12 The attenuation coefficients, μ (cm^{-1}), of the features inserted within the vulnerable plaque region: (1) CN, (2) FN, and (3) iodinated blood (IB), reconstructed using filtered back projection (FBP) with Ramp and Hanning filters.

individual energy-specific image and the spectral information across all energy images. In the first processing stage, each energy bin is computed to take account the signal and measurement noise distributed within the energy bin independently. Subsequently, the statistical and spectral information for all adjacent energy bins is integrated through the second processing stage using another template. Specifically, the correlation across the energy-specific images is calculated using a different covariance matrix of the intermediate scores obtained from the first stage. This covariance matrix decorrelates the image statistics scores and yields a spectral correlation matrix to be flat or white eigen-spectrum.¹⁶ The final SNR calculated in this step yields all possible spatio-spectral information and correlation within and across the consecutive spectral image bins, thereby increasing the discrimination performance.

It may be suggested that the proposed numerical observer and the material-discrimination framework can be applied to investigate or compare imaging systems with no limitation on the data dimensionality. The underlying reasons of the advantages of the proposed two-staged design were described in our previous work.⁴⁰ For spectral CT imaging, the proposed method can be extended to investigate volumetric 3-D or 4-D images (i.e., 3-D in space and 1-D in time), as the channel functions can be modified to support the increased dimensionality. Furthermore, MECT-PC has the ability to decompose more than two materials, as more than one K -edge contrast medium can be simultaneously imaged and distinguished using four or more energy thresholds or windows.^{9,59} In this case, the proposed framework can be extended to support multiclass discrimination tasks or multiple-decision L -class problem with $L > 2$, where the data are to be assigned to one of L possible hypotheses or the underlying classes. Thus, multiple discriminant functions and partitioning rules are required to support multiple material-classification tasks. The observer then makes decision D_i , deciding in favor of hypothesis H_i .¹⁶ The relevant study performed by He et al. has demonstrated the three-class task performance based on linear discrimination analysis.⁶⁰

There is some question as to whether increasing the number of energy bins of MECT-PC has significant impact on the FOM of the material classification or not. Leng et al. have shown that the selection of the number, width, and location of energy bins have influence in material differentiation and noise of spectral CT.³³ There is a tradeoff between energy bin size (or energy bin

number) and image noise. For example, a narrow energy bin has better energy resolution compared to a wider energy bin, and it enables better material differentiation. However, using narrow bins (imply more number of energy bins) allows smaller number of photons available in each energy bin, and therefore the image noise within each bin increases. Multiple energy bins provide more data points available along the attenuation-energy curve and enable better curve-fitting to promote better material differentiation. In contrast, the increased image noise may make it impossible to detect small differences in material composition. Therefore, the proposed numerical observer can be used to investigate the overall performance of the material differentiation with varying these parameters, as the proposed observer can assess both material specificity and image noise throughout multiple energy bins simultaneously.

We acknowledge as a limitation of this work that several assumptions are made to demonstrate the method as implemented for comparison of all the investigated CT systems. Our primary objective in this study is to present the development and validation of the observer models by means of simulation. Specifically, the aim of this study is to contribute to broadly used implemented technologies of spectral CT systems for both DECT and MECT. All the specific assumptions were consistently made to demonstrate the method implementation for comparison of all the investigated CT systems. In this study, the numerical observer framework has been carefully validated on simulated data where the ground truth is known and where the parameters (e.g., plaque feature types, feature size, feature location, equivalent radiation doses of all modalities) can be easily changed to study the impacts of their variation on the classification performance. In the literature, several research studies demonstrated and validated their methods on the assumptions of ideal detectors for investigating the performance of conventional CT and spectral CT.^{4,61,62} In order to model more realistic systems, it is suggested that our validation may apply decreased efficiency to the implementations of detectors and energy resolution for further investigation, especially for photon-counting spectral CT, e.g., applying 10% decrease in energy resolution with the quantum detection efficiency varying with photon energy⁴ or using 12% full width at half maximum energy resolution.⁶¹ In addition, a material decomposition method is suggested to apply to our data generation to include the possible variation that may obtain from the decomposition method.⁶³ These investigations can be separated validation studies.

For the future work, we will validate the performance of MECT in different detector designs with decreased efficiency of detectors as well as real acquisition data from a clinical scanner system using the proposed observer method. According to SKE/BKE (or SKS/BKE), the physical and statistical properties of the set of objects to be imaged may be specified with use of the simulation of material features one can provide the investigator with optimal methods for characterizing the properties of the objects. Adding simulated targets to real images (creating so-called hybrid images) becomes an interesting realistic option for task-based assessment studies.^{16,24,25,64} Hence, image fusion between the simulated plaque features and patient's background demonstrated in our framework may be appropriately applied in clinical validation. This simulation work, which is a pilot study for the assessment of spectral CT in plaque imaging, can be applied to other clinical applications, such as coronary artery plaque imaging, differentiation of kidney stones,⁶⁵ or identification of gouty tophi.⁶⁶

5 Conclusion

In this paper, we have proposed and validated a numerical observer with an image assessment framework for material discrimination tasks using spectral CT images. Our method overcomes the main limitation of the current quantitative metrics for evaluating spectral CT imaging, whose data domain is complex and multidimensional. The proposed observer has been designed to have two-step processing: first, accommodating the spatial attenuation information in each energy bin and, second, integrating all spatial-attenuation information to finally assess the material characteristics acquired from multiple energy windows of spectral CT. The proposed methods were evaluated using simulated data, in which attenuation coefficient maps were generated using XCAT and fused to the generated plaque features with known elemental compositions. Binary classification tasks, which are based on the standard SKE/BKE task and which mimic clinical scenarios with the variation of signal certainty based on the SKS/BKE task, were performed. Our methods showed the improvement of plaque classification tasks, which were measured by discrimination SNR and AUC FOM, using MECT systems as compared to the different acquisition methods of both DECT and conventional CT systems at equivalent dose. Our observer method would mimic the human observer perception for investigating multiple energy-specific images, which may possibly be a more accurate evaluation to assess the discrimination performance in clinical spectral CT practice.

Acknowledgments

This work was supported in part by Grant Nos. R01HL110241, R01CA165221, R01EB013293, and R01HL118261. The authors would like to thank Dr. Junguo Bian for his valuable suggestion in CT imaging. The contents of this article are solely the responsibility of the authors and do not represent the official views of the NIH.

References

1. F. Jashari et al., "Coronary and carotid atherosclerosis: similarities and differences," *Atherosclerosis* **227**(2), 193–200 (2013).
2. A. S. Go et al., "Heart disease and stroke statistics—2014 update: a report from the American Heart Association," *Circulation* **129**(3), e28–e292 (2014).
3. J. M. van Werkhoven et al., "Prognostic value of multislice computed tomography and gated single-photon emission computed tomography in patients with suspected coronary artery disease," *J. Am. Coll. Cardiol.* **53**(7), 623–632 (2009).
4. P. Baturin, Y. Alivov, and S. Molloy, "Spectral CT imaging of vulnerable plaque with two independent biomarkers," *Phys. Med. Biol.* **57**(13), 4117–4138 (2012).
5. P. Ibrahim et al., "Coronary and carotid atherosclerosis: how useful is the imaging?" *Atherosclerosis* **231**(2), 323–333 (2013).
6. M. Wintermark et al., "High-resolution CT imaging of carotid artery atherosclerotic plaques," *AJNR. Am. J. Neuroradiol.* **29**(5), 875–882 (2008).
7. T. T. de Weert et al., "In vivo characterization and quantification of atherosclerotic carotid plaque components with multidetector computed tomography and histopathological correlation," *Arterioscler. Thromb. Vasc. Biol.* **26**(10), 2366–2372 (2006).
8. T. R. C. Johnson, C. Fink, and S. O. Schonberg, *Dual Energy CT in Clinical Practice*, Springer-Verlag Berlin Heidelberg, Heidelberg Dordrecht London New York (2011).
9. K. Taguchi and J. S. Iwanczyk, "Vision 20/20: single photon counting x-ray detectors in medical imaging," *Med. Phys.* **40**(10), 100901 (2013).
10. B. Heismann, B. Schmidt, and T. Flohr, *Spectral Computed Tomography*, SPIE, Washington (2012).
11. T. De Zordo et al., "Comparison of image quality and radiation dose of different pulmonary CTA protocols on a 128-slice CT: high-pitch dual source CT, dual energy CT and conventional spiral CT," *Eur. Radiol.* **22**(2), 279–286 (2012).
12. A. M. Alessio and L. R. MacDonald, "Quantitative material characterization from multi-energy photon counting CT," *Med. Phys.* **40**(3), 031108 (2013).
13. Y. Rakvongthai et al., "Spectral CT using multiple balanced K-edge filters," *IEEE Trans. Med. Imaging* **34**(3), 740–747 (2015).
14. L. Boussel et al., "Photon counting spectral CT component analysis of coronary artery atherosclerotic plaque samples," *Br. J. Radiol.* **87**(1040), 20130798 (2014).
15. X. Wang, A. Zamyatin, and D. Shi, "Dose reduction potential with photon counting computed tomography," *Proc. SPIE* **8313**, 831349 (2012).
16. H. H. Barrett and K. J. Myers, *Foundations of Image Science*, Wiley-Interscience (2004).
17. K. J. Myers et al., "Effect of noise correlation on detectability of disk signals in medical imaging," *J. Opt. Soc. Am. A* **2**(10), 1752–1759 (1985).
18. R. D. Fiete et al., "Hotelling trace criterion and its correlation with human-observer performance," *J. Opt. Soc. Am. A* **4**(5), 945–953 (1987).
19. H. H. Barrett et al., "Model observers for assessment of image quality," *Proc. Natl. Acad. Sci. U. S. A.* **90**(21), 9758–9765 (1993).
20. J. P. Rolland and H. H. Barrett, "Effect of random background inhomogeneity on observer detection performance," *J. Opt. Soc. Am. A* **9**(5), 649–658 (1992).
21. H. Barret et al., "Stabilized estimates of hotelling-observer detection performance in patient structured noise," *Proc. SPIE* **3340**, 27–43 (1998).
22. A. E. Burgess, X. Li, and C. K. Abbey, "Visual signal detectability with two noise components: anomalous masking effects," *J. Opt. Soc. Am. A Opt. Image. Sci. Vision* **14**(9), 2420–2442 (1997).
23. H. C. Gifford et al., "Channelized hotelling and human observer correlation for lesion detection in hepatic SPECT imaging," *J. Nucl. Med.* **41**(3), 514–521 (2000).
24. G. El Fakhri et al., "Impact of acquisition geometry, image processing, and patient size on lesion detection in whole-body 18F-FDG PET," *J. Nucl. Med.* **48**(12), 1951–1960 (2007).
25. G. El Fakhri et al., "Improvement in lesion detection with whole-body oncologic time-of-flight PET," *J. Nucl. Med.* **52**(3), 347–353 (2011).
26. H. W. Tseng et al., "Assessing image quality and dose reduction of a new x-ray computed tomography iterative reconstruction algorithm using model observers," *Med. Phys.* **41**(7), 071910 (2014).
27. A. A. Sanchez, E. Y. Sidky, and X. Pan, "Task-based optimization of dedicated breast CT via Hotelling observer metrics," *Med. Phys.* **41**(10), 101917 (2014).
28. L. Saba et al., "Carotid artery plaque characterization using CT multi-energy imaging," *AJNR. Am. J. Neuroradiol.* **34**(4), 855–859 (2013).
29. D. P. Cormode et al., "Atherosclerotic plaque composition: analysis with multicolor CT and targeted gold nanoparticles," *Radiology* **256**(3), 774–782 (2010).
30. J. Paul et al., "Dual-energy CT spectral and energy weighted data sets: carotid stenosis and plaque detection," *Acad. Radiol.* **20**(9), 1144–1151 (2013).
31. R. Zainon et al., "Spectral CT of carotid atherosclerotic plaque: comparison with histology," *Eur. Radiol.* **22**(12), 2581–2588 (2012).
32. D. S. Rigie and P. J. L. Riviere, "Task based characterization of spectral CT performance via the hotelling observer," in *IEEE Nuclear Science Symp. (NSS) and Medical Imaging Conf. (MIC)* (2012).
33. S. Leng et al., "Noise reduction in spectral CT: reducing dose and breaking the trade-off between image noise and energy bin selection," *Med. Phys.* **38**(9), 4946–4957 (2011).
34. W. H. Sommer et al., "Image quality of virtual non-contrast images derived from dual energy CT angiography after endovascular aneurysm repair," *J. Vasc. Interv. Radiol.* **21**, 315–321 (2010).
35. P. Stolzmann et al., "Endoleaks after endovascular abdominal aortic aneurysm repair: detection with dual-energy dual-source CT," *Radiology* **249**(2), 682–691 (2008).
36. H. Chandarana et al., "Abdominal aorta: evaluation with dual-source dual-energy multidetector CT after endovascular repair of aneurysms—initial observations," *Radiology* **249**(2), 692–700 (2008).

37. L. Platasa et al., "Channelized Hotelling observers for the assessment of volumetric imaging data sets," *J. Opt. Soc. Am. A Opt. Image Sci. Vision* **28**(6), 1145–1163 (2011).
38. M. Chen et al., "Using the Hotelling observer on multislice and multi-view simulated SPECT myocardial images," *IEEE Trans. Nucl. Sci.* **49**(3), 661–667 (2002).
39. A. Lorsakul et al., "4D Mathematical model observer for lesion detection on respiratory-gated PET imaging," *J. Nucl. Med.* **54**(Suppl. 52), 538 (2013).
40. A. Lorsakul et al., "4D numerical observer for lesion detection in respiratory-gated PET," *Med. Phys.* **41**(10), 102504 (2014).
41. A. Lorsakul et al., "A numerical observer for task-based assessment on kinetic parametric imaging," *J. Nucl. Med.* **55**(Suppl. 51), 48 (2014).
42. A. Lorsakul et al., "Numerical observer for objective assessment on carotid plaque using spectral CT," in *IEEE Medical Imaging Conf. (MIC 2014)*, pp. 1–4, Seattle, Washington (2014).
43. L. Zhou, "Low-contrast lesion detection in tomosynthetic breast imaging," in *Electrical and Computer Engineering*, Stony Brook University (2007).
44. R. F. Wagner et al., "Finite-sample effects and resampling plans: Applications to linear classifiers and computer-aided diagnosis," *Proc. SPIE*, 467–477 (1997).
45. W. P. Segars et al., "4D XCAT phantom for multimodality imaging research," *Med. Phys.* **37**(9), 4902–4915 (2010).
46. R. A. Ribeiro et al., "Common carotid artery bifurcation levels related to clinical relevant anatomical landmarks," *Int. J. Morphol.* **24**(3), 413–416 (2006).
47. B. Heismann and M. Balda, "Quantitative image-based spectral reconstruction for computed tomography," *Med. Phys.* **36**(10), 4471–4485 (2009).
48. M. Yang, "Dual energy computed tomography for proton therapy treatment planning," in *The University of Texas, Health Science* (2011).
49. J. H. Hubbell and S. M. Seltzer, "Tables of x-ray mass attenuation coefficients and mass energy-absorption coefficients," <http://physics.nist.gov/PhysRefData/XrayMassCoef/cover.html>
50. Y. Z. O'Connor and J. A. Fessler, "Fourier-based forward and back-projectors in iterative fan-beam tomographic image reconstruction," *IEEE Trans. Med. Imaging* **25**(5), 582–589 (2006).
51. T. M. Buzug, *Computed Tomography From Photon Statistics to Modern Cone-Beam CT*, Springer-Verlag Berlin Heidelberg, Berlin Heidelberg (2008).
52. J. H. Siewerdsen et al., "Spektr: a computational tool for x-ray spectral analysis and imaging system optimization," *Med. Phys.* **31**(11), 3057–3067 (2004).
53. P. M. Shikhaliev and S. G. Fritz, "Photon counting spectral CT versus conventional CT: comparative evaluation for breast imaging application," *Phys. Med. Biol.* **56**(7), 1905–1930 (2011).
54. A. N. Primak et al., "Dual-source dual-energy CT with additional tin filtration: dose and image quality evaluation in phantoms and in vivo," *Am. J. Roentgenol.* **195**(5), 1164–1174 (2010).
55. J. Hsieh, *Computed Tomography Principles, Design, Artifacts, and Recent Advances*, 2nd ed., SPIE Press, Bellingham, Washington (2009).
56. D. T. Boll et al., "Spectral coronary multidetector computed tomography angiography: dual benefit by facilitating plaque characterization and enhancing lumen depiction," *J. Comput. Assist. Tomogr.* **30**(5), 804–811 (2006).
57. J. C. Schenzle, W. H. Sommer, and K. Neumaier, "Dual energy CT of the chest: how about the dose?" *Invest. Radiol.* **45**, 347–353 (2010).
58. B. Li, G. Yadava, and J. Hsieh, "Head and body CTDIw of dual energy x-ray CT with fast-kVp switching," in *SPIE Medical Imaging*, pp. 7622–7669, SPIE, San Diego, California (2010).
59. K. Kim et al., "Sparse-view spectral CT reconstruction using spectral patch-based low-rank penalty," *IEEE Trans. Med. Imaging* **34**(3), 748–760 (2015).
60. X. He and E. C. Frey, "The validity of three-class Hotelling trace (3-HT) in describing three-class task performance: comparison of three-class volume under ROC surface (VUS) and 3-HT," *IEEE Trans. Med. Imaging* **28**(2), 185–193 (2009).
61. Y. Alivov et al., "Optimization of K-edge imaging for vulnerable plaques using gold nanoparticles and energy resolved photon counting detectors: a simulation study," *Phys. Med. Biol.* **59**(1), 135–152 (2014).
62. T. G. Schmidt, K. C. Zimmerman, and E. Y. Sidky, "The effects of extending the spectral information acquired by a photon-counting detector for spectral CT," *Phys. Med. Biol.* **60**(4), 1583–1600 (2015).
63. M. Yveborg, M. Danielsson, and H. Bornefalk, "Theoretical comparison of a dual energy system and photon counting silicon detector used for material quantification in spectral CT," *IEEE Trans. Med. Imaging* **34**(3), 796–806 (2015).
64. J. Schaefferkoetter et al., "Clinical impact of time-of-flight and point response modeling in PET reconstructions: a lesion detection study," *Phys. Med. Biol.* **58**(5), 1465–1478 (2013).
65. A. Graser, R. T. Johnson, and M. Bader, "Dual energy CT characterization of urinary calculi: initial in vitro and clinical experience," *Invest. Radiol.* **43**, 112–119 (2008).
66. R. T. Johnson et al., "Clinical image: dual-energy computed tomographic molecular imaging of gout," *Arthritis Rheum.* **56**(8), 2809–2809 (2007).

Auranuch Lorsakul received her PhD in biomedical engineering from Columbia University, New York, in 2015 under the supervision of Dr. Andrew Laine. She was part of the Gordon Center for Medical Imaging under her thesis advisors, Drs. Georges El Fakhri and Quanzheng Li at MGH, Boston, Massachusetts, from 2012 to 2015. Currently, she is imaging scientist, imaging and algorithm, digital pathology at Roche Tissue Diagnostics. Her research interests include computer-aided diagnosis and state-of-the-art technologies in medical imaging.

Georges El Fakhri received his PhD in medical physics from University of Paris XI, France, in 1998. Currently, he is a professor of radiology at Harvard Medical School. He serves as the director of MGH PET Core, and Gordon Center. His research interests include quantitative methods in PET-CT and SPECT-CT, image generation and clinical task-based image assessment, quantitative simultaneous PET-MR, PET-CT and SPE-CT instrumentation, monitoring radiotherapy with PET, and pharmacokinetic modeling of physiological processes.

Andrew F. Laine received his Doctor of Science in computer science from Washington University, St. Louis, Missouri, in 1989. Currently, he is a professor of biomedical engineering and radiology at Columbia University. He serves as the chair of the Department of Biomedical Engineering and the director of the Heffner Biomedical Imaging Laboratory at Columbia University. His research interests include mathematical analysis and quantification of medical images, signal and image processing, and computer-aided diagnosis.

Quanzheng Li received his PhD in electrical engineering from the University of Southern California, Los Angeles, California, in 2005. Currently, he is an associate professor at Harvard Medical School and an associate physicist at Massachusetts General Hospital (MGH). His research interests include static and dynamic model-based image reconstruction of MRI, CT, and PET kinetic modeling of dynamic PET and MRI images, direct estimation of parametric image, and computer-aided diagnosis for small lesion detection.

Biographies for the other authors are not available.